Available online at www.sciencedirect.com

ScienceDirect

Geochimica et Cosmochimica Acta 207 (2017) 210–231

Geochimica et Cosmochimica Acta

www.elsevier.com/locate/gca

Influence of iron redox cycling on organo-mineral associations in Arctic tundra soil

Elizabeth Herndon [a,b,*], Amineh AlBashaireh [a,c], David Singer [a], Taniya Roy Chowdhury [d,1], Baohua Gu [b], David Graham [d]

[a] Department of Geology, 221 McGilvrey Hall, Kent State University, Kent, OH 44242, USA
[b] Environmental Sciences Division, Oak Ridge National Laboratory, P.O. Box 2008, MS-6036, Oak Ridge, TN 37831, USA
[c] Department of Geology, College of Wooster, Wooster, OH 44691, USA
[d] Biosciences Division, Oak Ridge National Laboratory, Oak Ridge, TN 37831, USA

Received 7 July 2016; accepted in revised form 26 February 2017; Available online 25 March 2017

Abstract

Arctic tundra stores large quantities of soil organic matter under varying redox conditions. As the climate warms, these carbon reservoirs are susceptible to increased rates of decomposition and release to the atmosphere as the greenhouse gases carbon dioxide (CO_2) and methane (CH_4). Geochemical interactions between soil organic matter and minerals influence decomposition in many environments but remain poorly understood in Arctic tundra systems and are not considered in decomposition models. The accumulation of iron (Fe) oxyhydroxides and organo-iron precipitates at redox interfaces may be particularly important for carbon cycling given that ferric iron [Fe(III)] species can enhance decomposition by serving as terminal electron acceptors in anoxic soils or inhibit microbial decomposition by binding organic molecules. Here, we examine chemical properties of solid-phase Fe and organic matter in organic and mineral horizons within the seasonally thawed active layer of Arctic tundra on the North Slope of Alaska. Spectroscopic techniques, including micro-X-ray fluorescence (μXRF) mapping, micro-X-ray absorption near-edge structure (μXANES) spectroscopy, and Fourier transform infrared spectroscopy (FTIR), were coupled with chemical sequential extractions and physical density fractionations to evaluate the spatial distribution and speciation of Fe-bearing phases and associated organic matter in soils.

Organic horizons were enriched in poorly crystalline and crystalline iron oxides, and approximately 60% of total Fe stored in organic horizons was calculated to derive from upward translocation from anoxic mineral horizons. Ferrihydrite and goethite were present as coatings on mineral grains and plant debris, and in aggregates with clays and particulate organic matter. Minor amounts of ferrous iron [Fe(II)] were present in iron sulfides (i.e., pyrite and greigite) in mineral horizon soils and iron phosphates (vivianite) in organic horizons. Concentrations of organic carbon in the organic horizons (28 ± 5 wt.% C) were approximately twice the concentrations in the mineral horizons (14 ± 2 wt.% C), and organic matter was dominated by base-extractable and insoluble organics enriched in aromatic and aliphatic moieties. Conversely, water-soluble organic molecules and organics solubilized through acid-dissolution of iron oxides comprised <2% of soil organic C and were consistent with a mixture of alcohols, sugars, and small molecular weight organic acids and aromatics released through decomposition of larger molecules. Integrated over the entire depth of the active layer, soils contained 11 ± 4 kg m^{-2} low-density, particulate organic C and 19 ± 6 kg m^{-2} high-density, mineral-associated organic C, indicating that 63 ± 19% of organic C in the active layer was associated with the mineral fraction.

We conclude that organic horizons were enriched in poorly crystalline and crystalline iron oxide phases derived from upward translocation of dissolved Fe(II) and Fe(III) from mineral horizons. Precipitation of iron oxides at the redox interface

* Corresponding author at: 221 McGilvrey Hall, Department of Geology, Kent State University, Kent, OH 44242, USA.
E-mail address: eherndo1@kent.edu (E. Herndon).
[1] Present address: Biological Sciences Division, Pacific Northwest National Laboratory, Richland, WA 99352, USA.

http://dx.doi.org/10.1016/j.gca.2017.02.034

has the potential to contribute to mineral protection of organic matter and increase the residence time of organic carbon in arctic soils. Our results suggest that iron oxides may inhibit organic carbon degradation by binding low-molecular-weight organic compounds, stabilizing soil aggregates, and forming thick coatings around particulate organic matter. Organic matter released through acid-dissolution of iron oxides could represent a small pool of readily-degradable organic molecules temporarily stabilized by sorption to iron oxyhydroxide surfaces. The distribution of iron in organic complexes and inorganic phases throughout the soil column constrains Fe(III) availability to anaerobic iron-reducing microorganisms that oxidize organic matter to produce CO_2 and CH_4 in these anoxic environments. Future predictions of carbon storage and respiration in the arctic tundra should consider such influences of mineral stabilization under changing redox conditions.

Keywords: Iron; Soil organic matter; Arctic; Tundra

1. INTRODUCTION

Average annual temperatures at high-latitudes are increasing more quickly than the global average and driving pronounced shifts in hydrology, vegetation, and decomposition of soil organic matter in Arctic ecosystems (Hinzman et al., 2013; Pachauri et al., 2014). Decades of increasing soil temperatures have led to extensive thaw of near-surface permafrost and altered landscape drainage (Osterkamp and Romanovsky, 1999; Yoshikawa and Hinzman, 2003; Jorgenson et al., 2006), while increasing rates of evapotranspiration are shrinking lakes and drying out surface soils in tundra and boreal wetlands (Yoshikawa and Hinzman, 2003; Smith et al., 2005; Riordan et al., 2006). These processes are expected to generate warmer and drier conditions across substantial portions of Arctic and sub-Arctic ecosystems with pockets of increased soil saturation (Hinzman et al., 2013). Hydrologic conditions control redox gradients that impact pathways of organic matter decomposition and carbon storage in soils (e.g., Vonk et al., 2015; Schädel et al., 2016). Given that permafrost-affected soils in circumpolar regions store vast quantities of belowground organic carbon (~1300 Pg; Hugelius et al., 2014), enhanced C release as carbon dioxide (CO_2) and methane (CH_4) under warmer temperatures may result in a substantial positive feedback to climate change. Increasing temperatures accelerate decomposition by stimulating microbial activity (Davidson and Janssens, 2006) and by thawing frozen organic substrates (Schuur et al., 2009). Organic matter that is currently stored under anoxic conditions may undergo rapid aerobic decomposition as saturated soils are drained (Huemmrich et al., 2010; Elberling et al., 2013), while inundated areas may serve as heightened sources of methane (Turetsky et al., 2008; Zona et al., 2009; Lipson et al., 2012; Olefeldt et al., 2013).

Although substantial research has been geared toward understanding how the organic matter stored in high-latitude peatlands will decompose under warming climate (e.g., Pachauri et al., 2014 and refs. therein), few studies have examined the geochemistry of redox-sensitive elements in these systems. Specifically, studies describing Fe geochemistry in tundra and boreal soils remain sparse (e.g., Fiedler et al., 2004; Lipson et al., 2010; Sundman et al., 2014), while studies that focus on Fe—C dynamics in soil pore waters and stream networks are more abundant (e.g., Pokrovsky and Schott, 2002; Pokrovsky et al., 2006, 2016; Ilina et al., 2013; Page et al., 2013). Iron and C cycles are coupled through numerous processes that include anaerobic respiration of organic matter (Lovely and Phillips, 1986; Roden and Wetzel, 1996; Lipson et al., 2010), mineral protection of organic substrates (Gu et al., 1994, 1995; Kleber et al., 2005; Lalonde et al., 2012; Riedel et al., 2012), and nutrient P bioavailability to plants and microorganisms (Borggaard et al., 1990; Jensen et al., 1992; Bjerrum and Canfield, 2002). It is especially critical to understand the role of Fe in mineral-stabilization of organic matter given that mineral protection in addition to chemical recalcitrance may largely control its long-term degradability (Baldock and Skjemstad, 2000; Lutzow et al., 2006; Lehmann and Kleber, 2015). Thus, it is necessary to address the paucity of information regarding Arctic Fe biogeochemistry given that Fe may serve a critical role in regulating the C source or sink potential of high-latitude ecosystems.

Iron geochemistry in soils is regulated by redox conditions induced by soil saturation and microbial respiration. In well-drained soils that remain oxic, Fe that is released from silicate minerals during chemical weathering precipitates as Fe(III) oxyhydroxides such as goethite and hematite (Schwertmann, 2008). In poorly drained soils that experience periodic or persistent anoxia, microorganisms reduce ferric oxides to generate magnetite (Lovley et al., 1987) or release Fe(II) into solution where it can either leach from the soil or diffuse to oxic zones and precipitate as poorly crystalline ferrihydrite (Zak et al., 2004; Riedel et al., 2012). In the absence of oxygen, Fe(II) can combine with sulfide (S-rich, low pH environment), phosphate (high PO_4^{3-}), or carbonate species (high pH environment) to form secondary pyrite (FeS_2), vivianite ($Fe_3(PO_4)_2{\cdot}8H_2O$), or siderite ($FeCO_3$) phases (Roden and Edmonds, 1997; Borch et al., 2010). The relative importance of these processes have not been examined in the arctic tundra; thus, we provide baseline characterization of Fe geochemistry in tundra soils in order to evaluate Fe cycling and Fe-organic interactions.

Extensive regions of high-latitude landscapes are persistently or intermittently saturated peatlands, generating redox gradients that are conducive to dynamic Fe geochemistry. Indeed, flocculates of iron oxide precipitates are commonly observed in standing pools of water in tundra and boreal systems (e.g., Emerson et al., 2015). Iron-oxidizing bacteria capitalize on the slow kinetics of Fe(II) oxidation in these cold and organic-rich environments to form thick microbial mats at redox interfaces (Theis and Singer,

1974; Emerson et al., 2015). Oxidation of Fe(II) at redox interfaces generates radical oxygen species that enhance organic matter decomposition (Hall and Silver, 2013; Page et al., 2013), facilitating the breakdown of complex plant biopolymers to produce labile substrates for microbial respiration reactions (Herndon et al., 2015b; Yang et al., 2016). Accumulations of solid-phase Fe(III) also provide an abundant terminal electron acceptor for microbial respiration during periods of anoxia (Lovely and Phillips, 1986). Although researchers have begun to investigate anaerobic Fe(III) respiration in Arctic systems (Lipson et al., 2010, 2013; Miller et al., 2015; Roy Chowdhury et al., 2015), less is known regarding solid-phase Fe-organic associations. Poorly crystalline iron oxyhydroxides may protect organic compounds from degradation by forming stable mineral-organic associations through sorption, aggregation, or co-precipitation reactions (e.g., Gu et al., 1994, 1995; Kleber et al., 2005; Wiseman and Püttmann, 2006; Lalonde et al., 2012; Riedel et al., 2012; Cismasu et al., 2016). Conversely, organic molecules can suppress iron oxyhydroxide precipitation by complexing dissolved Fe(III) and inhibiting hydrolysis (Karlsson et al., 2008; Karlsson and Persson, 2010; Sundman et al., 2014), or can sorb onto poorly crystalline ferrihydrite and inhibit transition to crystalline goethite or magnetite minerals (e.g., Schwertmann and Murad, 1988; Schwertmann, 2008; Cismasu et al., 2011; Amstaetter et al., 2012). Thus, the geochemistry of Fe and organic matter are strongly intertwined in such systems (Prietzel et al., 2007; Sundman et al., 2014).

Despite the important role Fe plays in Arctic biogeochemistry, Fe speciation in the solid-phase of tundra soils has not been thoroughly examined. Although previous studies have attributed high Fe concentrations in organic horizons to mineral inputs from cryoturbation or changing water tables (Lipson et al., 2010; Hobara et al., 2013), high Fe/Ti ratios suggest that Fe enrichment in organic soils occurs independent of mineral particles (Fiedler et al., 2004; Herndon et al., 2015a). We previously concluded that Fe reduction deep in the mineral horizon of the seasonally thawed active layer produces Fe(II) that migrates upwards in the soil profile and is oxidized to Fe(III)-oxyhydroxide minerals and organically-complexed Fe(III) in the organic horizon (Herndon et al., 2015a). Here, we use sequential chemical extractions and synchrotron-source X-ray microprobe techniques to examine solid-phase Fe in organic and mineral horizons contained within the seasonally thawed active layer. Additional chemical extractions and physical fractionation techniques are coupled with Fourier-transform infrared spectroscopy (FTIR) to quantify and characterize mineral-associated organic C.

2. METHODS

2.1. Site description

Arctic ecosystem response to climate change has been investigated at the Barrow Environmental Observatory (BEO) on the Arctic Coastal Plain of Alaska as part of the Next Generation Ecosystem Experiment (NGEE) – Arctic project (Wullschleger et al., 2011; http://ngee.ornl.gov). The BEO, located approximately 5 km southeast of Barrow, AK, is dominated by lakes and interlake patterned ground formed by ice-wedge polygons (Hubbard et al., 2013). Polygons exhibit microtopographic features that regulate hydrologic flow paths and generate sharp redox gradients across small spatial scales (Lipson et al., 2010; Zona et al., 2011). Low-centered polygons consist of depressed center basins that are bordered by elevated rims and depressed troughs, while high-centered polygons consist of elevated center mounds surrounded by depressed troughs. Soils in the polygons consist of thin (<20 cm) to thick (20–40 cm) organic horizons overlying gleyed, silty lacustrine deposits that contain abundant ground ice and have been mixed to varied degrees through cryoturbation (Brown et al., 1980; Bockheim et al., 2001). The maximum depth of the seasonally thawed active layer ranges from approximately 20 to 60 cm across the interstitial polygons and is generally greatest below the troughs (Hubbard et al., 2013). The landscape receives little annual precipitation but is largely saturated due to underlying permafrost that restricts soil drainage (Bockheim et al., 2001).

This study examines iron and organic carbon geochemistry in organic and mineral horizon soils from low-centered and high-centered polygons in an interstitial area at BEO (Wullschleger et al., 2011; Hubbard et al., 2013). Soils in this area are classified as Typic Aquiturbels or Typic Histoturbels and are characterized by high organic content, moderate to poor drainage, and cryoturbation features (Bockheim et al., 2001). Frozen soil cores were collected from trough, ridge, and center positions of the low-centered polygon and from trough and center positions of the high-centered polygon in April 2012. A Snow, Ice, and Permafrost Research Establishment coring auger (manufactured by Jon's Machine Shop in Fairbanks, AK) mounted on a sled was used to collect ~1 m length soil cores in clear PVC liners (3″ diameter times 36″ length) that were sterilized with ethanol prior to use. Soil cores were kept frozen during shipment to and storage at Oak Ridge National Laboratory. Previous studies on these soils are reported by Roy Chowdhury et al. (2015), Herndon et al. (2015a), and Herndon et al. (2015b).

2.2. Geochemical analyses

Frozen soil cores were removed from their liners under N_2 atmosphere in a vinyl anaerobic chamber (Coy Laboratory Products) to maintain anoxic conditions. Soils consisted of intermediately decomposed (Oe) to highly decomposed (Oa) organic horizons of varying thickness (range 8–30 cm) overlying organic-rich, gleyed mineral horizons (Bgh) (Chowdhury and Graham, 2013; Roy Chowdhury et al., 2015). Soil pH in 1 M potassium chloride ranged from 4.5 to 6.3 (Roy Chowdhury et al., 2015). Ground ice was present at the bottom of all cores, and layers containing predominantly ice were excluded from further processing. The depth to ground ice was roughly coincident with the maximum thaw depth at each site (Herndon et al., 2015a); therefore, the soil investigated here was predominantly within the seasonally thawed active

layer. Each core was sectioned into organic and mineral horizons which were thawed and homogenized in an autoclaved plastic bucket using an oscillating power tool with sterilized cutting blades. Subsamples of the homogenized soil horizons were weighed into 50 ml Falcon tubes, refrozen at −20 °C, and freeze-dried for 48 h prior to subsequent analysis. Soil water content was quantified as the mass loss from frozen soil during freeze-drying and was consistent with values obtained from replicate samples that were dried overnight at 105 °C. Soil organic carbon (SOC) and organic nitrogen were quantified by combustion following acidification (LECO TruSpec CN Determinator). Soil bulk density (ρ_b) of each horizon was estimated as a function of SOC following Bockheim et al. (2003), where $\ln \rho_b$ (g cm^{-3}) = −[SOC(%) − 8.24]/9.79 (Table 1). Calculated bulk densities were consistent with measured values reported by Iversen et al. (2015) for soils collected from nearby polygons in the BEO (Fig. A1). All further steps were performed under air unless otherwise specified.

Sequential extractions targeting exchangeable (Fe_{exch}), poorly crystalline oxide (Fe_{ox1}), crystalline oxide (Fe_{ox2}), magnetite (Fe_{mag}), and organic-bound (Fe_{org}) Fe fractions were performed on organic and mineral soils from the low-centered and high-centered polygons using methods adapted from Tessier et al. (1979), Amacher et al. (1990), and Poulton and Canfield (2005). All solutions were prepared with 18 MΩ water in acid-washed labware. Extraction of exchangeable Fe (loosely bound to organics and mineral surfaces) was performed in the anaerobic chamber (N_2 atmosphere with ~2% H_2). Briefly, 10 ml of N_2-degassed 0.1 M $BaCl_2$-NH_4Cl solution was added to ~0.5 g freeze-dried soil and mixed for 20 min on a mechanical rotator. The slurry was centrifuged at 4000*g* for 30 min to pelletize the sediment, and the supernatant was filtered (<0.45 μm nylon syringe filter) into 50 ml metal-free Falcon tubes and acidified with 2–3 drops of concentrated ultrapure nitric acid. Poorly crystalline iron oxides (e.g., ferrihydrite, lepidocrocite) were extracted with 1 M hydroxylamine-hydrochloride in 25% v/v acetic acid for 48 h. Crystalline iron oxides (e.g., goethite, hematite) were extracted with freshly-prepared citrate-buffered sodium dithionite (50 g l^{-1} in 0.35 M acetic acid + 0.2 M sodium citrate buffer solution at pH 4.8) for 2 h. Extraction of magnetite, which may also extract ilmenite and metals complexed with humic acid-like polymers (McKeague, 1967; Siregar et al., 2005), was performed using 0.2 M ammonium oxalate + 0.17 M oxalic acid solution at pH 3.2 for 6 h. Finally, the oxidizable Fe fraction, which consists primarily of organic-bound Fe (strongly complexed by organics or present in biomass) but could include minor quantities of sulfide minerals, was extracted for ~10 h with periodic agitation at 85 °C with hydrogen peroxide (30%), nitric acid, and 3.2 M ammonium acetate in 20% (v/v) nitric acid (Tessier et al., 1979). The residual fraction contained primarily silicate minerals and insoluble organic matter. Between each step, soils were rinsed by vortexing the pellet with 10 ml of 0.01 M potassium chloride solution, centrifuging to collect supernatant, and combining the filtered rinse solution with the extract. Relative standard error of duplicate extractions was <25% for Fe_{exch}, <7% for Fe_{ox1}, <12% for Fe_{ox2}, <11% for Fe_{mag}, and <29% for Fe_{org}. Extract solutions were stored at 4 °C until analysis of Fe by inductively coupled plasma optical emission spectrometry (ICP-OES) using matrix-specific calibration standards. Extract solutions that were not reacted with soil were analyzed as method blanks to assess potential contamination from extract chemicals. Concentrations of extracted Fe in each fraction are reported per mass of dry soil.

Density fractionation was used to quantify particulate organic carbon present as free organic matter (low-density) and as mineral-associated or occluded organic matter (high-density) (Swanston et al., 2005; Crow et al., 2007).

Table 1
Concentration (μmol g^{-1}) and relative percentage (% of total) of extractable Fe in soils collected from organic (O) and mineral (M) horizons in the active layer of low-centered polygons (LCP) and high-centered polygons (HCP).

Core ID	Depth cm	Bulk density[a] g cm^{-3}	Water content g H_2O g soil^{-1}	Fe_{exch} μmol g^{-1} (%)	Fe_{ox1} μmol g^{-1} (%)	Fe_{ox2} μmol g^{-1} (%)	Fe_{mag} μmol g^{-1} (%)	Fe_{org} μmol g^{-1} (%)
LCP-Ridge-O	0–8	0.04	3.67	7.0 (1.6)	284 (64)	135 (30)	13 (3.0)	4.3 (1.0)
LCP-Ridge-M	8–46	0.52	0.79	2.1 (3.1)	31 (46)	13 (19)	5.1 (7.5)	16.6 (24)
LCP-Trough-O	0–19	0.29	2.48	11 (3.6)	166 (55)	68 (23)	15 (4.9)	41.7 (14)
LCP-Trough-M	25–69	1.03	0.74	2.0 (2.0)	56 (56)	16 (16)	10 (10)	16.3 (16)
LCP-Center-O	0–22	0.05	9.62	15 (6.9)	121 (57)	65 (30)	13 (6.2)	0.5 (0.2)
LCP-Center-M	22–54	0.57	0.64	2.6 (1.7)	71 (48)	28 (19)	15 (9.8)	32.9 (22)
HCP-Center-O	0–20	0.45	0.70	2.6 (1.5)	107 (63)	32 (19)	9.8 (5.7)	19.3 (11)
HCP-Center-M	20–50	0.44	0.75	3.7 (3.3)	60 (52)	20 (18)	8.8 (7.7)	21.7 (19)
HCP-Trough-O	0–30	0.19	1.95	5.7 (3.5)	100 (62)	39 (24)	6.9 (4.3)	9.1 (5.7)
HCP-Trough-M	30–50	0.52	0.84	4.5 (3.5)	66 (52)	24 (19)	11 (8.6)	22.4 (18)
Organic horizons, average				8.2 (3.4)	155 (60)	68 (25)	12 (4.8)	15 (6.4)
Organic horizons, standard error				2.1 (1.0)	34 (2)	18 (2)	1.5 (0.6)	7 (2.7)
Mineral horizons, average				3.0 (2.7)	57 (51)	20 (18)	10.0 (8.8)	22 (20)
Mineral horizons, standard error				0.5 (0.4)	7 (2)	3 (1)	1.6 (0.5)	3 (2)
p-value[b]				*0.12 (0.68)*	*0.04 (0.05)*	*0.04 (0.05)*	*0.55 (0.04)*	*0.36 (0.04)*

[a] Bulk density (ρ_b) calculated as $\ln \rho_b$ = −[SOC (%) − 8.24]/9.79 (Bockheim et al., 2003).
[b] *p*-value indicates significant differences between organic and mineral horizons (≤0.05).

Approximately 30–35 ml of 1.66 g ml^{-1} low carbon, sodium polytungstate (SPT) solution (Sometu, Germany) was added to ~5–10 g of bulk freeze-dried soil in a 50 ml Falcon tube to yield a minimum 1:4 soil to SPT ratio. The exact mass of dry soil used in each fractionation was quantified following freeze-drying and varied depending on initial water content. Each tube was vortexed thoroughly to mix, then let sit at room temperature for 24–48 h until low-density matter (float) clearly separated from high-density matter (sink). Float material was carefully decanted onto a glass fiber filter (0.7 μm) and rinsed with ultrapure water until the density of the rinsed solution reached ~1 g ml^{-1}. The sink material was rinsed of residual SPT by repeatedly mixing with ultrapure water, centrifuging, and decanting the supernatant. Negligible quantities of low-density organic matter were liberated during the rinsing procedure. Density fractionation was performed in duplicate on a subset of samples to obtain methodological error (<20%).

Each fraction was either dried in an oven overnight at 60 °C or freeze-dried. A small portion of each density fraction from low-centered polygon soils was analyzed for C and N content by combustion (LECO TruSpec CN Determinator). Organic carbon contents in density fractions of the high-centered polygon soils were estimated by the loss on ignition (LOI) at 550 °C and a linear relationship between SOC and LOI established for the low-centered polygon soils (see below). Soluble organics that remained in solution following fractionation were not analyzed. Soil mineral content was defined as the weight percent of each soil with a bulk density greater than 1.66 g cm^{-3}.

A sequential chemical extraction procedure was used to isolate organic compounds based on their solubility in water (water-extractable organic C; WEOC), acid (acid-extractable organic C; AEOC), and base solutions (base-extractable organic C; BEOC) (Ryan et al., 1990; Boyer and Groffman, 1996; Jandl and Sollins, 1997; Hishi et al., 2004; Hobara et al., 2013). Approximately 1 g of lightly-ground, freeze-dried soil was weighed into a 50 ml Falcon tube and sequentially extracted with 20 ml of 0.01 M potassium chloride at pH 4.5 to obtain WEOC, followed by 0.1 M hydrochloric acid to obtain AEOC, then 0.1 M sodium hydroxide to obtain BEOC. These operationally-defined pools represent readily soluble, low-molecular-weight organic compounds (WEOC), organic compounds released through proton-promoted dissolution of iron oxides (AEOC), and base-soluble and mineral-associated C (BEOC). The residual insoluble organic matter, which is operationally-equivalent to humin, is chemically complex and undefined. All soils were obtained during initial processing of the soil cores, with the exception of one sample (low-centered polygon center organic horizon) that was extracted following anoxic incubation for 30 days, as detailed by Roy Chowdhury et al. (2015), because no pre-incubation material was available. Quantities of WEOC and AEOC increased following incubation (Herndon et al., 2015a), thus this sample was excluded from quantification of these two fractions.

Soil samples were mixed with each extract solution at 60 rpm on a benchtop rotator for ~20 h. After mixing, the tubes were centrifuged for 30 min at 7000*g*, and the supernatant was decanted into a Falcon collection tube. Soils were rinsed after each extraction by vortexing with ~10 ml 0.01 M KCl, centrifuging for 20 min at 7000*g*, and decanting the supernatant into the collection tube. The rinse step was completed twice for the water and acid extractions and three times for the base extraction. For the base extraction, all steps were completed in a glove box under N_2 to prevent oxidation reactions. After the third rinse step, the base extract was neutralized to pH ~ 7 with hydrochloric acid before being removed from the glove box. Extract solutions were vacuum-filtered through 0.45 μm Supor polyethersulfone membranes. Due to a high concentration of particulates that were solubilized with sodium hydroxide, the base extracts were diluted with ultrapure water prior to filtration. We define the material filtered out of the base extracts (>0.45 μm) as "base-soluble particulates" and quantify base-soluble particulate C as the difference between soil organic carbon and the sum of WEOC, AEOC, BEOC, and residual C. All organic extracts were stored at 4 °C until analysis. Duplicate extractions were performed on high-centered polygon samples to assess technical replication. Relative standard deviation of duplicate extractions was <3% for WEOC and AEOC, <12% for BEOC, and <7% for residual C.

Dissolved organic carbon concentrations for each organic extract were analyzed on a Shimadzu TOC-5000 and reported as mass of organic carbon per mass of dry soil (mg C g^{-1} soil). Subsamples of the freeze-dried residuals were combusted for 4 h at 550 °C to measure loss on ignition (LOI), which was converted to C concentration using the regression equation obtained from the LOI and % C established for the LCP soils (% C = 0.41 * LOI + 5.7; $R^2 = 0.97$ and standard error = 2.4%) which is consistent with reported relationships between SOC and LOI (Pribyl, 2010).

Soil properties for each horizon are reported as the average ± standard error of sampled soils. Effects of soil horizon (organic or mineral) on soil properties were tested at a significance level $\alpha = 0.05$ using the nonparametric Kruskal–Wallis ANOVA with a Benjamini-Hochberg correction for multiple comparisons (Benjamini and Hochberg, 1995). Statistical tests were performed using R statistical programming language (R version 3.2.5). Linear regression analyses were performed in SPSS®.

2.3. Mass balance approach to quantify Fe inputs to organic horizons

A mass balance approach was used to calculate the relative proportions of Fe in the organic horizon derived from particle mixing and upward translocation of solutes by comparing concentrations of Fe in mineral ($C_{Fe,B} = 225 \pm 58$ mmol kg^{-1}) and organic ($C_{Fe,org} = 359 \pm 6$ mmol kg^{-1}) soils with concentrations of the relatively inert element Ti (Brimhall and Dietrich, 1987; Neaman et al., 2006) in mineral ($C_{Ti,B} = 48.5 \pm 9.0$ mmol kg^{-1}) and organic ($C_{Ti,B} = 27 \pm 7.1$ mmol kg^{-1}) soils. Here, we used an average soil composition reported for the low-centered polygon by Herndon et al. (2015a). Although

colloidal Ti can be mobile in redox-active environments (Thompson et al., 2006), exchangeable Ti comprised <0.25% and extractable Ti comprised <5% of total Ti in these soils (Table A1), indicating that Ti was primarily present in chemically recalcitrant mineral phases.

Rock-derived elements in the mineral (B) horizon are contained in particles that include quartz, aluminosilicates, iron oxides, etc. In the organic horizon, mineral elements derive from either inputs of these particles through mixing with the mineral soil via cryoturbation (Kaiser et al., 2007) or precipitation of secondary minerals and organic-complexes following upward translocation of solutes (Fiedler et al., 2004). For the purpose of this model, we assume that elements are translocated from the mineral horizon to the organic horizon and that inputs to and outputs from the active layer are comparatively negligible.

Area-normalized concentrations of constituent j (m_j; mmol m^{-2}) can be calculated for each horizon as follows:

$$m_j = C_{j,\text{horizon}} \times \rho \times d \quad (1)$$

Here, m_j (mmol m^{-2}) is the area-normalized mass of constituent j (e.g., j = Fe), $C_{j,\text{horizon}}$ (mmol kg^{-1}) is the concentration of j in the homogenized soil horizon for a given fraction, ρ (kg m^{-3}) is the average bulk density of the soil horizon (Table 1), and d (m) is the soil horizon thickness. For a mobile element such as Fe, the area-normalized mass of that element in the organic horizon ($m_{\text{Fe,org}}$; mmol m^{-2}) is the sum of masses translocated through diffusion or convection and mixing:

$$m_{\text{Fe,org}} = m_{\text{Fe,diff}} + m_{\text{Fe,mix}} \quad (2)$$

$F_{\text{Fe,diff}}$ and $F_{\text{Fe,mix}}$ denote the area-normalized masses of Fe (mmol m^{-2}) input to the organic horizon through diffusion or convection and mixing processes, respectively. Immobile elements such as Ti are poorly-soluble and are transported primarily as particles through mixing; thus, $m_{\text{Ti,diff}} = 0$ and $m_{\text{Ti,org}} = m_{\text{Ti,mix}}$. Due to translocation of elements from the mineral to the organic horizon, elements in the B horizon are depleted relative to their parent mineralogy by an amount equal to their mass in the organic horizon. Thus, the area-normalized mass of an element j in the B horizon at a given time ($m_{j,B}$; mmol m^{-2}) is equal to the area-normalized mass of j prior to any translocation ($m^0_{j,B}$; mmol m^{-2}) minus the translocated mass ($m_{j,\text{org}}$):

$$m_{j,B} = m^0_{j,B} - m_{j,\text{org}} \quad (3)$$

Mineral particles that enter the organic horizon through mixing are similar in composition to the mineral horizon at time zero. The concentration of an element in the mineral soil at time zero ($C^0_{j,B}$) is calculated by substituting Eq. (1) into Eq. (3) and rearranging to yield:

$$C^0_{j,B} = C_{j,B} + C_{j,\text{org}}\left(\frac{\rho_{\text{org}} d_{\text{org}}}{\rho_B d_B}\right) \quad (4)$$

Here, ρ_{org} (=200 ± 80 kg m^{-3}) and ρ_B (=610 ± 100 kg m^{-3}) are the average (±standard error) bulk densities of the organic and mineral horizons respectively, and d_{org} (=0.20 ± 0.04 m) and d_B (=0.33 ± 0.04 m) are the average depth intervals recorded each horizon. Averaged across all soils, $C^0_{\text{Fe},B} = 296 \pm 93$ mmol kg^{-1} and $C^0_{\text{Ti},B} = 54 \pm 12$ mmol kg^{-1}.

The immobile element Ti can be used to determine the total mass of soil particles input to the organic horizon through mixing (m_{mix}; kg m^{-2}):

$$m_{\text{Ti,mix}} = m_{\text{Ti,org}} = m_{\text{mix}} C^0_{\text{Ti},B} \quad (5)$$

According to this equation, all Ti in the organic horizon is contained in particles with a total mass m_{mix} and an average concentration of $C^0_{\text{Ti},B}$. The quantity m_{mix} is calculated by substituting Eq. (1) into Eq. (5) and rearranging:

$$m_{\text{mix}} = (C_{\text{Ti,org}}/C^0_{\text{Ti},B})\rho_{\text{org}} d_{\text{org}} \quad (6)$$

Unlike Ti, Fe is introduced to the organic horizon through both particle mixing and solute translocation pathways. The amount of Fe in the organic horizon derived from upward translocation is equal to the total mass of Fe in the organic horizon minus the proportion derived from physical mixing:

$$m_{\text{Fe,diff}} = m_{\text{Fe,org}} - m_{\text{mix}} C^0_{\text{Fe},B} \quad (7)$$

The quantity of particles input through mixing was previously determined using concentrations of immobile Ti (Eq. (6)). Therefore, we substitute Eqs. (1) and (6) into Eq. (7) and rearrange to solve for $m_{\text{Fe,diff}}$:

$$m_{\text{Fe,diff}} = \rho_{\text{org}} d_{\text{org}}[C_{\text{Fe,org}} - C^0_{\text{Fe},B}(C_{\text{Ti,org}}/C^0_{\text{Ti},B})] \quad (8)$$

The proportion of excess Fe in the organic horizon derived from diffusion or convection is determined as:

$$Fe_{\text{diff}}(\%) = 100 \times (m_{\text{Fe,diff}}/m_{\text{Fe,org}}) \quad (9)$$

Uncertainty in reported values were calculated as the propagated error for element concentrations, bulk density, and soil depth across all soils.

2.4. Spectroscopic analyses

The microscale distribution and speciation of Fe in all soils was investigated with synchrotron-source X-ray microprobe techniques, including micro-X-ray fluorescence (μXRF) mapping, micro-X-ray absorption near edge structure (μXANES) spectroscopy, and micro-X-ray diffraction (μXRD), at GSECARS 13-ID-E at the Advanced Photon Source at Argonne National Laboratory. Soils from the organic and mineral horizons of all topographic positions in the low- and high-centered polygons (n = 10) were analyzed in February 2015. Samples were prepared for analysis by spreading a thin layer of freeze-dried powder on X-ray transmissive Kapton tape. Micro-XRF maps were collected using a 1.5 × 1.5 μm focused beam at 7100 eV and ~6.0 × 10^{11} s^{-1} flux with a 3 μm step size and 30 ms dwell time. X-ray absorption spectra were collected from −50 to +250 eV around the Fe K-edge (E0 = 7111 eV) for points of interest identified in all maps.

Freeze-dried soils from the organic and mineral horizons of the low-centered polygon trough were shipped to Spectrum Petrographic (Vancouver, WA) for thin section preparation. Soils were embedded in EPO-TEK 301-2FL resin, prepared as standard (30 μm thick) thin sections, and

mounted on high-purity quartz-glass slides. Initial imaging, elemental mapping, and spot quantification of element stoichiometry was completed for these thin sections using scanning electron microscopy with energy dispersive X-ray spectroscopy (SEM-EDS) on a Hitachi TM3030 Tabletop microscope with a Bruker Quantax 70 Plus Elemental X-ray Analysis system. Organic matter was identified as either low-contrast biological structures or biological structures with associated high-contrast elements (e.g., Fe), while minerals were identified as high-contrast grains that contained rock-derived elements (e.g., Si, Ti, Fe, Al).

Microprobe analyses on these thin sections were completed at GSECARS 13-ID-E in July 2015 (Table A2). Micro-XRF maps were collected with a 1.5×1.5 μm focused beam at 18,000 eV and $\sim 3.7 \times 10^{10}$ s^{-1} flux with a 2 μm step size and 50 ms dwell time. X-ray absorption spectra were collected from −50 to +250 eV around the Fe K-edge (E0 = 7111 eV) for points of interest identified in all maps. Micro-XRD patterns were collected in transmission geometry using a CCD area detector with the incident beam energy set at 18 keV. Fe redox mapping was performed by collecting maps at 7110 eV, 7117 eV, 7123 eV, 7127 eV, 7136 eV, and 7147 eV. Fe(II) distribution maps were constructed from the I0-normalized map at 7123 eV, given that Fe(II) is dominant in the μXAS spectra at this energy. The total Fe distribution (Fe_T) was based on the map at 7136 eV, as there is negligible difference in the absorption intensity of Fe(II) and Fe(III) at this energy. The distribution of Fe(III) was therefore determined as the difference between Fe_T and Fe(II). Quantitative analysis using linear combination fits of μXANES spectra at specific map locations was used to confirm the procedure to determine the spatial distribution of Fe(II) and Fe(III).

Micro-XRF maps were compiled in MapViewer v.8 (Larch version 0.9.24). Linear combination fits (LCFs) on μXANES spectra were performed in Athena software following energy calibration, merging of replicate scans, background subtraction, and normalization (Ravel and Newville, 2005). All samples were energy calibrated when necessary to align with the reference library such that E0 = 7110.7 eV for an Fe foil (Kraft et al., 1996). To determine average Fe valence state, LCFs were performed from −20 to +30 eV around the Fe K-edge using a library of single-valence Fe standards that included $FeCl_3$, FeO, goethite, siderite, hematite, $FeSO_4$, akaganeite, pyrite, and 2-line ferrihydrite reported by the Advanced Light Source, Lawrence Berkeley National Laboratory. X-ray diffraction images were processed with DIOPTAS software (Prescher and Prakapenka, 2015) using CeO_2 as a standard for geometrical calibration and the epoxy-coated slide for background subtraction. Mineral phase identification was performed using JADE 6.5 (Materials Data Inc., Livermore, CA).

Chemical properties of organic matter in chemical extractions and density fractions were evaluated using Fourier transform infrared (FTIR) spectroscopy (Table A2). FTIR spectra were obtained from 4000 to 800 cm^{-1} at 2 cm^{-1} steps on a Nicolet Magna 760 spectrophotometer equipped with a liquid nitrogen cooled MCT (mercury-cadmium-tellurium) detector. Extract solutions were deposited on IR transparent ZnSe windows and dried in an oven at 60 °C prior to analysis. For dilute extracts with low dissolved organic matter, samples were concentrated by depositing multiple layers on the window prior to analysis. For solid samples, including physical fractions and extract residuum, small portions (~3 mg) of powdered samples were ground with ~200 mg oven-dried KBr and pelletized using a hydraulic press. All spectra were background corrected to either a clean ZnSe window or to a pure KBr pellet. The peak positions (cm^{-1}) and absorbance intensities (peak heights) relative to the baseline were determined following baseline subtraction using Thermo Nicolet OMNIC v7.3 software. Indices examined include the ratios of maximum absorbance in regions representing hydroxyl O—H (3350–3400 cm^{-1}), aliphatic C—H (~2935 cm^{-1}), carbonyl C=O (~1740 cm^{-1}), aromatic C=C and deprotonated carboxylate C=O (1590–1650 cm^{-1}), and polysaccharide C—O (1030–1070 cm^{-1}) functional groups (e.g., Solomon et al., 2005; Hay and Myneni, 2007).

3. RESULTS

3.1. Iron geochemistry

Vertical gradients in Fe geochemistry were explored by comparing average concentrations of extracted Fe between organic and mineral horizons across all sites. Total concentrations of extractable Fe were higher in organic (258 ± 52 μmol g $soil^{-1}$) than mineral horizons (112 ± 14 μmol g $soil^{-1}$) ($p < 0.05$). Poorly crystalline iron oxyhydroxides (Fe_{ox1}) comprised the majority of extracted iron in all soils, while less Fe was present in crystalline, organic-bound, magnetite, and exchangeable fractions (Fig. 1a). Organic horizons contained higher concentrations of poorly crystalline (156 ± 34 μmol g $soil^{-1}$) and crystalline (68 ± 18 μmol g $soil^{-1}$) Fe than mineral soils (57 ± 7 μmol g $soil^{-1}$ and 20 ± 3 μmol g $soil^{-1}$, respectively) ($p < 0.05$). Additionally, the percentage of Fe present in poorly crystalline (60 ± 2%) and crystalline (25 ± 2%) iron oxides was higher in organic than mineral horizons (51 ± 2% and 18 ± 1%, respectively), while mineral horizons contained higher proportions of magnetite (Fe_{mag} = 8.8 ± 1.2%) and organic-bound Fe (Fe_{org} = 19.8 ± 3.3%) than organic horizons (4.8 ± 1.3% and 6.4 ± 6.1%, respectively) ($p < 0.05$) (Fig. 1b).

Area-normalized Fe contents (m_{Fe}; mmol m^{-2}) were calculated to compare pools of Fe in organic and mineral horizons (Eq. (1)). For the low-centered polygon soils analyzed in the mass balance calculations (Section 2.3), organic horizons stored less total Fe ($m_{Fe,org}$ = 14.4 ± 5.7 mol m^{-2}) than mineral horizons ($m_{Fe,org}$ = 51.3 ± 16.9 mol m^{-2}). Upward translocation ($m_{Fe,diff}$ = 8.4 ± 5.0 mol m^{-2}) rather than physical mixing contributed 59 ± 43% of total Fe stored in organic horizons (Eq. (8)). Within each soil core, the mineral horizon also contained larger pools of all Fe fractions than the organic horizon (Table A3), although differences in storage of extractable Fe between mineral and organic horizons were negligible when averaged across all sites ($p > 0.05$).

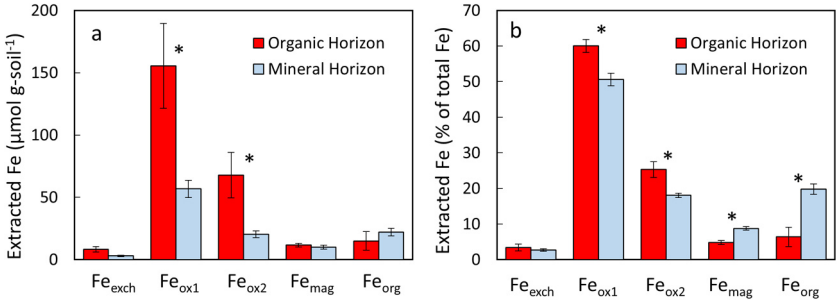

Fig. 1. (a) Concentrations of Fe (μmol g^{-1}) in organic or mineral horizon soils extracted as exchangeable (Fe_{exch}), poorly crystalline oxide (Fe_{ox1}), crystalline oxide (Fe_{ox2}), magnetite (Fe_{mag}), or organic-bound (Fe_{org}) iron. (b) Percentage of extracted iron present in each fraction. For all plots, columns and error bars represent the average and standard error for each fraction averaged across all organic (orange bars) or mineral horizons (blue bars). Asterisks denote significant differences between organic and mineral horizons ($p < 0.05$). Molar concentrations are reported per gram of dry soil. (For interpretation of the references to colour in this figure legend, the reader is referred to the web version of this article.)

3.2. Soil organic carbon

Organic horizons consisted primarily of low-density material (62 ± 18 wt.%), i.e., "free" particulate organic matter, while mineral horizons consisted primarily of high-density material (84 ± 6 wt.%), i.e., minerals, organic matter bound to minerals, and organic matter occluded in aggregates (Table 2) (Kögel-Knabner et al., 2008). Organic horizons contained an average ~2× more soil organic carbon (28 ± 5 wt.% SOC) and ~5× more low-density organic carbon (197 ± 61 mg C g $soil^{-1}$) than mineral horizons (13.5 ± 1.5 wt.% SOC and 42 ± 20 mg C g $soil^{-1}$ low-density C, respectively), but had highly variable proportions of high-density C (between <1% and 88% of total SOC). Concentrations of high-density C increased with increasing mineral content ($R^2 = 0.98$; Fig. 2a). On average, concentrations of organic carbon in the high-density fraction, defined here as mineral-associated C, were similar between organic (53 ± 28 mg C g $soil^{-1}$) and mineral (78 ± 15 mg C g $soil^{-1}$) horizons.

The area-normalized quantities of low-density and mineral-associated organic C were calculated for each soil horizon using Eq. (1) (Table 2). Organic horizons contained 4.8 ± 2.0 kg m^{-2} low-density C and 3.9 ± 2.4 kg m^{-2} high-density C, while mineral horizons contained 6.7 ± 3.9 kg m^{-2} low-density C and 15.5 ± 4.7 kg m^{-2} high-density C. Integrating over depth and averaging across all cores, we calculated that soils in the active layer contained 11 ± 4 kg m^{-2} low-density organic C and 19 ± 6 kg m^{-2} high-density organic C. This result indicates that 63 ± 19% of organic C in the active layer was associated with the mineral fraction.

Table 2
Concentrations of organic carbon in physical density fractionations in organic (O) or mineral (M) horizons of soils from low-centered (LCP) or high-centered (HCP) polygons.

Soil sample	SOC wt.%	LDF[a] wt.%	HDF[b] wt.%	LDF-C[c] mg g^{-1}	HDF-C[d] mg g^{-1}	LDF-C[3] wt.%	HDF-C[4] wt.%	LDF-C kg m^{-2}	HDF-C kg m^{-2}
LCP-Ridge-O	38.9	92	8	325	<DL	100	<DL	1.0	0.0
LCP-Ridge-M	14.6	40	60	108	24	82	18	21	4.7
LCP-Trough-O	20.5	39	61	100	92	52	48	5.5	5.1
LCP-Trough-M	8.0	4	96	<DL	72	<DL	100	0.0	33
LCP-Center-O	38.3	99	1	329	<DL	100	<DL	3.6	0.0
LCP-Center-M	13.8	10	90	<DL	84	<DL	100	0.0	15
HCP-Center-O	16.1	5	95	20	141	12	88	1.8	13
HCP-Center-M	16.4	16	84	57	106	35	65	7.6	14
HCP-Trough-O	24.4	74	26	212	32	87	13	12	1.8
HCP-Trough-M	14.6	12	88	43	103	29	71	4.4	10.8
Organic, average	27.6	62	38	197	53	70	30	4.8	3.9
Organic, std.err.	4.7	18	18	61	28	17	17	2.0	2.4
Mineral, average	13.5	16	84	42	78	29	71	6.7	15.5
Mineral, std.err.	1.4	6	6	20	15	15	15	3.9	4.7
p-value[e]	*0.05*	*0.18*	*0.18*	*0.14*	*0.55*	*0.14*	*0.14*		

[a] LDF = low-density soil fraction (% of total soil mass).
[b] HDF = high-density soil fraction (% of total soil mass).
[c] LDF-C = low-density soil C (mg g $soil^{-1}$ or % of total SOC).
[d] HDF-C = high-density soil C (mg g $soil^{-1}$ or % of total SOC).
[e] *p*-value indicates significant differences between organic and mineral horizons (<0.05).

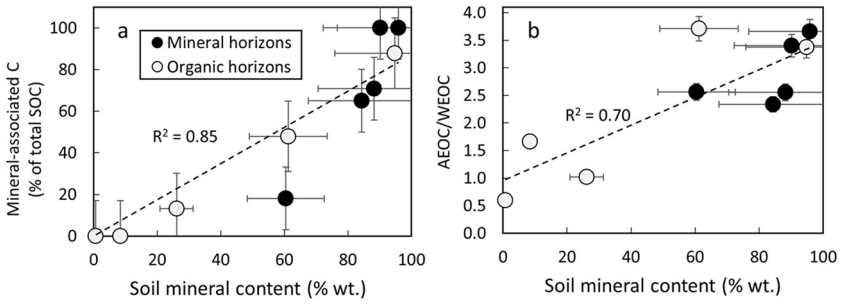

Fig. 2. (a) The proportion of organic carbon associated with minerals increases with increasing soil mineral content (wt.% of bulk dry soil), i.e., the high-density soil fraction, across all organic (white symbols) and mineral horizons (black symbols). (b) Organic carbon sorbed to iron oxide surfaces, quantified as acid-extractable organic carbon (AEOC), increased relative to water-extractable organic carbon (WEOC) with increasing soil mineral content. Linear regressions are highly significant ($p < 0.005$). Error bars in both plots indicate method uncertainty established for density fractionations (<20%) and chemical extractions (<3% for WEOC and AEOC).

Organic horizons contained higher concentrations of water- (WEOC), acid- (AEOC), and base-extractable (BEOC) organic carbon than mineral horizons (Table 3). To minimize differences generated by the total abundance of organic carbon, the percentage of extracted carbon present in each fraction was evaluated. There were no significant differences in the proportions of organic C present in each fraction between horizons; however, the ratio of AEOC to WEOC increased with increasing soil mineral content across all soils (Fig. 2b). WEOC and AEOC represent <2% of SOC and are comprised of labile organic compounds that are easily solubilized in water (WEOC) or sorbed to surfaces of minerals such as iron-oxides (AEOC); thus, sorption may increase as mineral surfaces become more abundant. Mineral horizons contained more C as base-soluble particulate-C ($52 \pm 8\%$ versus $35 \pm 11\%$) ($p < 0.05$), which is consistent with higher proportions of mineral-associated C in mineral horizons as measured by density fractionations.

FTIR spectra were distinct between each operationally defined pool but similar across all soils for a given fraction (Fig. 3). WEOC and AEOC were dominated by peaks for hydroxyl (O—H) functional groups with smaller peaks for aromatic-C and deprotonated carboxylate groups (C=C + C=O), polysaccharide-C (C—O), and aliphatic-C (C—H) groups (Fig. 3a and b). In contrast, BEOC was dominated by aromatic-C and exhibited prominent peaks for aliphatic-C and conjugated carbonyl (C=O) functional groups (Fig. 3c). Polysaccharide-C could not be assessed in BEOC samples due to a prominent Si—O stretching band ($\sim$1000 cm^{-1}) resulting from base-extracted silica groups. A subset of filtered and non-filtered base extracts was compared, and no difference between the FTIR spectra was observed except for a reduction in the peak at $\sim$1040 cm^{-1} in the filtered sample, presumably due to the removal of silicate particles. Particulate (low-density) and insoluble (residual) organic matter were dominated by O—H and C—O functional groups but also contained strong aliphatic-C and aromatic-C absorption bands

Table 3
Concentrations of organic carbon in chemical extractions from organic (O) or mineral (M) horizons of soils from low-centered (LCP) or high-centered (HCP) polygons.

Soil sample	SOC wt.%	WEOC mg g^{-1}	AEOC mg g^{-1}	BEOC mg g^{-1}	BSP-C mg g^{-1}	Residual C mg g^{-1}	WEOC %	AEOC %	BEOC %	BSP-C %	Residual C %
LCP-Ridge-O	38.9	2.1	3.5	114	105	165	0.54	0.90	29	27	42
LCP-Ridge-M	14.6	0.4	1.0	31	72	42	0.26	0.67	21	49	28
LCP-Trough-O	20.5	0.8	2.8	74	83	44	0.37	1.39	36	41	22
LCP-Trough-M	8.0	0.2	0.9	14	53	12	0.30	1.10	17	66	15
LCP-Center-O	38.3	8.1	4.9	95	72	203	2.11	1.27	25	19	53
LCP-Center-M	13.8	0.4	1.4	28	64	44	0.31	1.05	21	46	32
HCP-Center-O	16.1	0.6	2.0	55	64	39	0.37	1.24	34	40	24
HCP-Center-M	16.4	0.8	1.9	40	79	41	0.50	1.18	25	48	25
HCP-Trough-O	24.4	2.1	2.1	55	114	70	0.85	0.87	23	47	29
HCP-Trough-M	14.6	0.5	1.3	33	71	40	0.36	0.92	23	49	27
Organic, average	27.6	2.7	3.1	79	88	104	0.85	1.13	29	35	34
Organic, std.err.	4.7	1.4	0.5	12	9.5	34	0.33	0.10	3	5	6
Mineral, average	13.5	0.5	1.3	29	68	36	0.35	0.98	21	52	26
Mineral, std.err.	1.4	0.1	0.2	4.4	4.4	6	0.04	0.09	1	4	3
p-value[a]	*0.05*	*0.06*	*0.05*	*0.05*	*0.18*	*0.17*	*0.07*	*0.46*	*0.07*	*0.05*	*0.53*

[a] *p*-value indicates significant differences between organic and mineral horizons (<0.05).

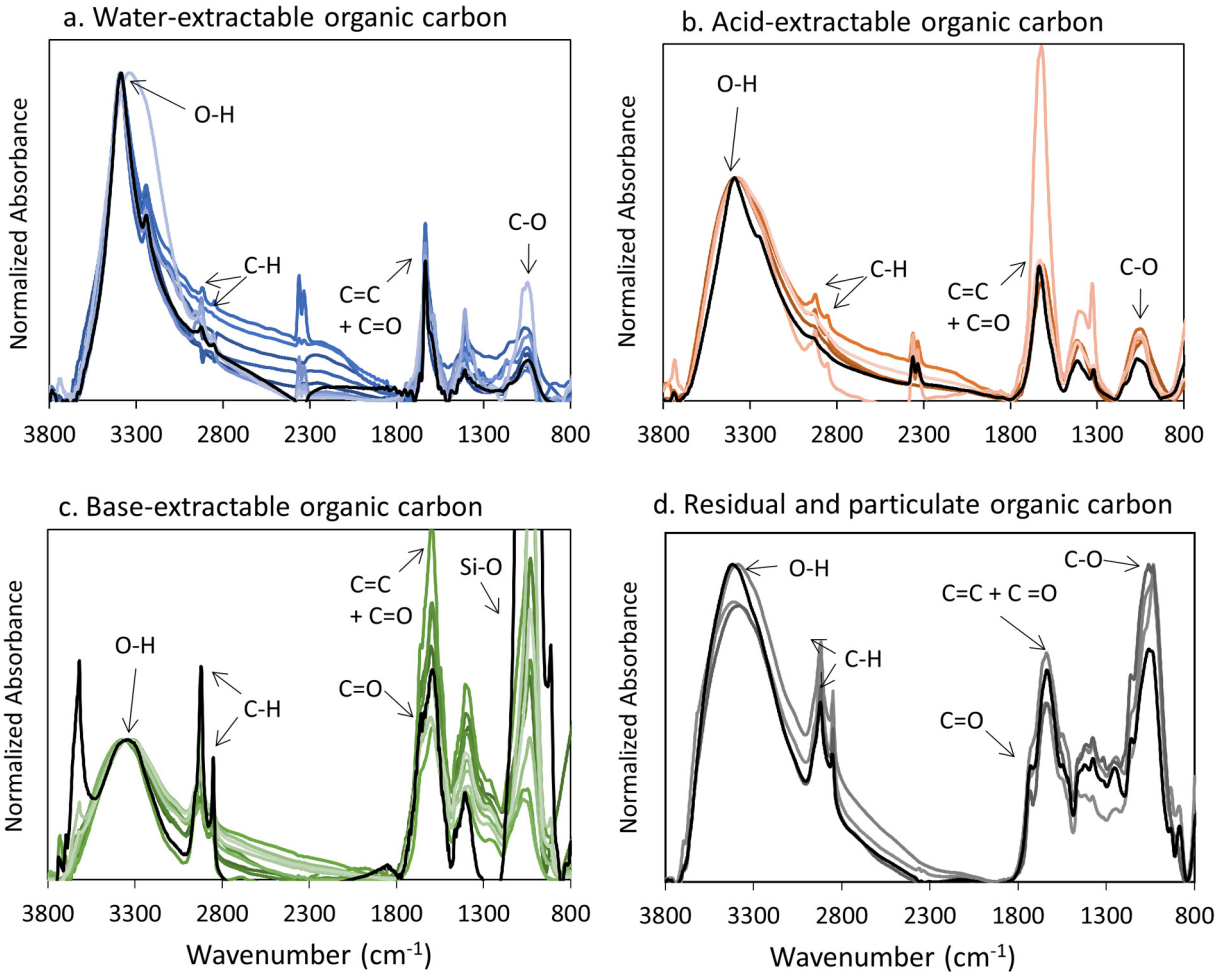

Fig. 3. Fourier-transform infrared spectra collected on (a) water-extractable, (b) acid-extractable, (c) base-extractable, and (d) low-density (<1.6 g cm^{-3}) and residual organic carbon phases from both organic and mineral soils of low-centered and high-centered polygons. Major absorption bands correspond to hydroxyl O—H (3350–3400 cm^{-1}), aliphatic C—H (~2935 cm^{-1}), carbonyl C═O (~1740 cm^{-1}), aromatic C═C and carboxylate C═O (1590–1650 cm^{-1}), and polysaccharide C—O (1030–1070 cm^{-1}) functional groups. A strong absorption band at ~1000 cm^{-1} in the alkaline extract (c) derives from the Si—O group of solubilized silica. One spectrum in each panel is outlined in black to emphasize patterns displayed by the remaining spectra (shown in varying shades of color to differentiate individual spectra). High-density and mineral-rich residual fractions were not included in panel (d) due to the dominance of the Si—O peak. (For interpretation of the references to colour in this figure legend, the reader is referred to the web version of this article.)

(Fig. 3d), consistent with an abundance of cellulose (dominated by hydroxyl and polysaccharide C—O) mixed with lignin (enriched in aromatic-C) and plant waxes and/or microbial lipids (aliphatic C—H). Spectra for high-density fractions were similar to residual and low-density fractions; however, the Si—O band from silicate minerals swamped absorption bands for organic groups below ~1400 cm^{-1}.

Spectroscopic indices were used to further examine differences among chemical extracts and physical fractions of organic matter (Fig. A3). Peak heights for carbonyl-C (1740 cm^{-1}) and hydroxyl (3350 cm^{-1}) groups were normalized to aromatic-C and carboxylate-C (1640 cm^{-1}) bands. WEOC and AEOC were chemically similar but distinct from BEOC, which was relatively enriched in carbonyl groups but depleted in hydroxyl groups. All chemically-extracted organic matter was depleted in carbonyl groups (1740 cm^{-1}/1640 cm^{-1} < 0.2) relative to residual and particulate organic matter (1740 cm^{-1}/1640 cm^{-1} > 0.3). High-density C was similar to residual and low-density C but exhibited a lower abundance of hydroxyls and carbonyls relative to aromatic-C and carboxylate C—O, yielding lower peak ratios of 3350 cm^{-1}/1640 cm^{-1} (1.0 ± 0.2 versus 1.4 ± 0.1) and 1740 cm^{-1}/1640 cm^{-1} (0.43 ± 0.05 versus 0.51 ± 0.4).

3.3. Microscale characterization

Detailed microscale analyses of Fe distribution and speciation were completed on thin sections of organic and mineral horizon soils from the low-centered polygon trough. The organic horizon consisted of agglomerations of low-contrast organic matter mixed with sand-sized or smaller high-contrast mineral grains (Fig. 4). The abundance of mineral grains was consistent with the observation that this

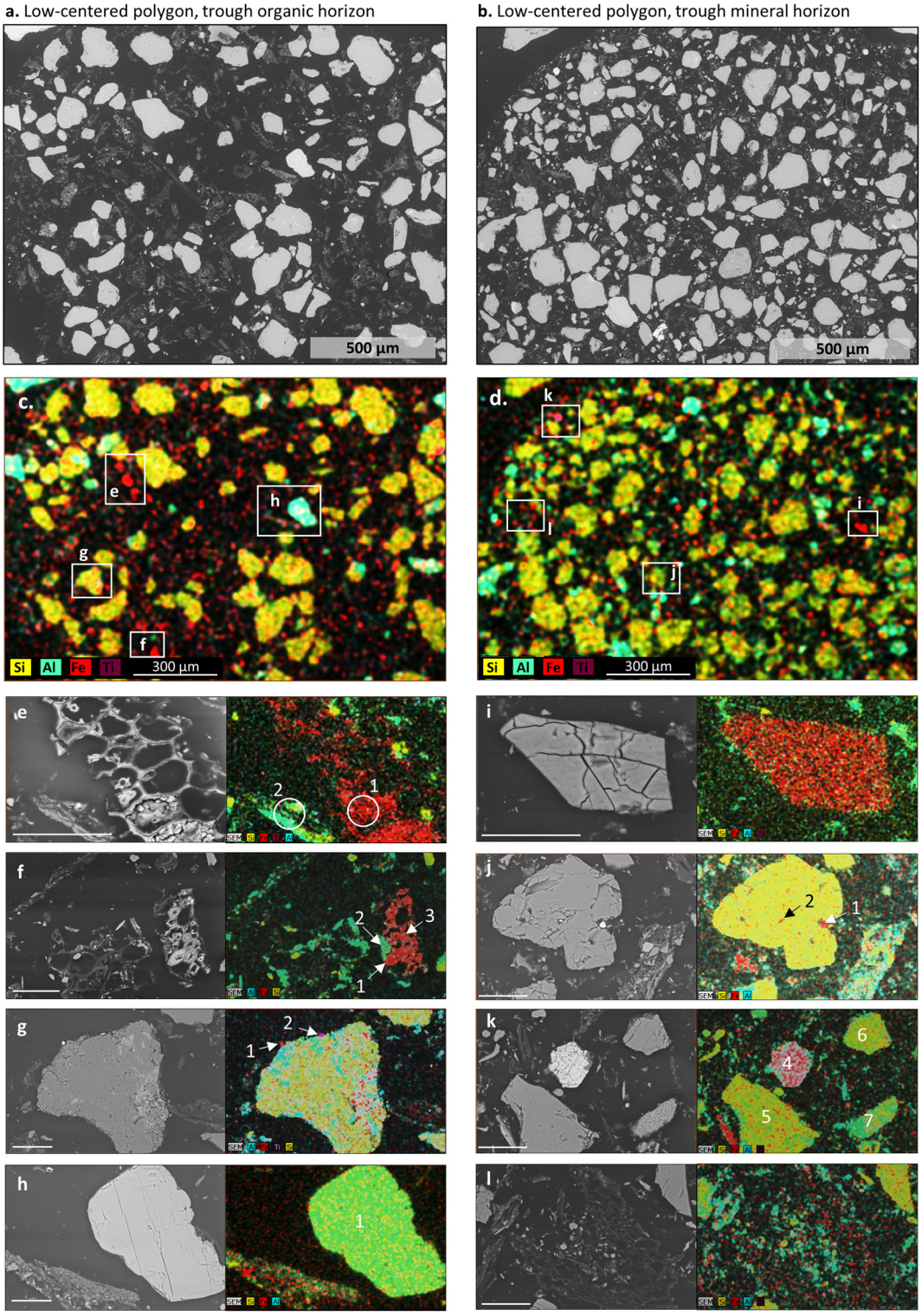

Fig. 4. Scanning electron microscopy (SEM) images of soil from the organic (a) and mineral (b) horizons of the low-centered polygon trough. Corresponding elemental maps of Si (yellow), Al (blue), Fe (red), and Ti (purple) (panels c and d) were obtained with energy-dispersive X-ray spectroscopy (EDS). Boxes in (c) and (d) indicate the positions of SEM (left panel) and EDS (right panel) maps shown in (e) through (l). Element stoichiometries, measured as atomic % in areas indicated by numbered circles and arrows, are reported in Table A4. Scale bars in panels (e) through (l) are 30 µm. (For interpretation of the references to colour in this figure legend, the reader is referred to the web version of this article.)

organic horizon contained a large percentage of high-density material (61 wt.%). Most mineral grains were comprised primarily of Si, consistent with quartz, while fewer contained both Si and Al, consistent with aluminosilicates such orthoclase ($KAlSi_3O_8$; Fig. 4h) and Al-oxide precipitates coated on quartz grains (Fig. 4g; Fig. A4). Ti was present in small (<5 μm) titanium-oxide particles (Fig. 4g) and in equal proportions to Fe in a few larger particles identified as ilmenite ($FeTiO_3$) (Fig. A5). Organic matter was often aggregated with micron-sized particles containing either Si and Al or Fe, presumed to be clays and iron-oxides. Iron was also observed in coatings on plant cells (Fig. 4e and f) and minerals (Figs. 4g and A2), or as small (<5 μm) discrete iron-oxide particles (Fig. 4g).

The mineral horizon of the low-centered trough contained a higher proportion of sand and aluminosilicate grains than the organic horizon (Fig. 4d), consistent with a higher percentage of high-density material (~96%). Although fragments of organic matter and organo-mineral aggregates were mixed in with the minerals, the organic C content was low (8.0 wt.% C) and presumed to be almost entirely mineral-associated given that very little low-density material (<5% of the soil mass) could be recovered during density fractionation. The mineral horizon contained Fe-bearing particles that included a few larger (~50 μm) Fe-rich silicates (Fig. 4i) and many small iron-oxides aggregated with clays and organic matter (Fig. 4j and 6l). Two small grains of iron sulfides (<5 μm diameter) with stoichiometries consistent with pyrite (1Fe:2S) and greigite (3Fe:4S) were observed on one large quartz grain (Fig. 4j). These were the only sulfides identified by SEM-EDS and no iron sulfide grains were observed with μXANES or μXRD (see below); therefore, iron sulfides may be only a minor soil constituent that form in highly-anoxic soils at depth. The specific depth within the horizon at which the observed sulfides formed could not be determined because the horizon was homogenized prior to analysis.

Iron speciation was further investigated in these soils using synchrotron-source microprobe techniques. In the organic horizon of the low-centered trough, Fe was present as Fe(II)-bearing minerals, Fe(III) oxides, and diffuse coatings on mineral grains and organic matter that consisted of a mixture of Fe(II) and Fe(III) (Figs. 5 and S5a). One especially Fe-rich grain ($Fe/I_0 = 11$) that also contained abundant Ti contained a mixture of Fe(II) and Fe(III) phases with an average valence of +2.2 (Fig. 5; spot A). X-ray diffraction patterns from this grain contained peaks for quartz, aluminosilicates (chlorite, kaolinite, muscovite, feldspar), and goethite, consistent with a large aggregate of quartz and clays cemented by iron oxide (Fig. 6). This aggregate also contained the Fe(II)-phosphate mineral vivianite. Other Fe-rich regions ($Fe/I_0 = 1.2–1.7$) contained >88% Fe(III) with an average valence of +2.9 (Fig. 5 and Table 4; spots C and G). Quartz, kaolinite, and muscovite, but no crystalline iron minerals, were identified by XRD for these spots, consistent with the presence of silicate minerals coated by poorly crystalline Fe(III) oxyhydroxides. Fe also appeared as coatings on particulate organic matter and mineral grains identified as quartz and aluminosilicates (Fig. 5; spots B, E, F, and H). These regions contained $55 \pm 8\%$ Fe(III) with an average valence of 2.6 ± 0.1 and were relatively Fe-poor ($Fe/I_0 < 0.6$), with the exception of one spot (Fig. 5a, spot B; $Fe/I_0 = 4.1$) that was located on the edge of the Fe-rich aggregate. Iron in these coatings is likely dominated by poorly crystalline iron oxyhydroxides given that no crystalline Fe oxides were detected with the exception of goethite at one spot (Fig. 6, spot H). Vivanite was also detected in these diffuse coatings (Fig. 6, spots B and H). Similar to soils in the organic horizon, soils in the mineral horizon of the low-centered polygon trough contained a mix of Fe(II) and Fe(III) species, including goethite, associated with quartz and aluminosilicates (Figs. 7 and A6–A7); however, vivianite was not detected. Additional μXAS spectra ($n = 56$) collected on freeze-dried soil powders also exhibited a mix of Fe(II) and Fe(III) species consistent with Fe(II)- and Fe(III)-oxides standards, but not siderite ($FeCO_3$) or pyrite (FeS_2) (Figs. A8–A9).

4. DISCUSSION

4.1. Iron geochemistry

Poorly crystalline iron oxyhydroxides (e.g., ferrihydrite) dominated non-silicate Fe phases in all soils and comprised $60 \pm 4\%$ of extractable Fe in organic horizons (Fig. 1), likely forming the Fe-rich precipitates associated with minerals and plant debris (Fig. 4). Crystalline iron oxides such as goethite comprised between 15% and 30% of extractable Fe (Table 1) and were present in aggregates with clay and organic matter (Figs. 5 and 6). Crystalline iron oxide content (% Fe_{ox2}) was strongly, positively correlated with soil organic C (wt.%) across all soils ($R^2 = 0.97$; $p < 0.001$). Although organic compounds can inhibit the transition from poorly crystalline ferrihydrite to crystalline goethite or magnetite minerals (e.g., Schwertmann and Murad, 1988; Schwertmann, 2008; Amstaetter et al., 2012), organic horizons are near the land surface where higher dissolved oxygen levels and fluctuating redox conditions may increase the rate of crystallization (Thompson et al., 2006). Release of molecular oxygen from plant roots into the subsurface may contribute to the dominance of iron oxide phases in these soils despite periodic to persistent conditions of anoxia. Indeed, Fe-plaques formed abiotically and by Fe-oxidizing bacteria are commonly observed to coat roots of wetland plants (Emerson et al., 1999; Hansel et al., 2001). Plant uptake of iron is normally low, limited to biosynthetic requirements. However, some plants have been reported to hyperaccumulate metal ions, including iron in root and shoot tissues, which could promote iron accumulation in litter. The mechanism and ecological distribution of plant hyperaccumulation remains to be investigated.

High concentrations of organic matter and acidic conditions (pH ~ 4.5–6.3) at the redox interface may favor organic complexation of Fe(III) ion species at the partial expense of iron oxyhydroxide precipitation (Wagai and Mayer, 2007; Karlsson et al., 2008; Karlsson and Persson, 2010; Sundman et al., 2014). Organic molecules stabilize both Fe(III) and iron oxyhydroxides that form at redox

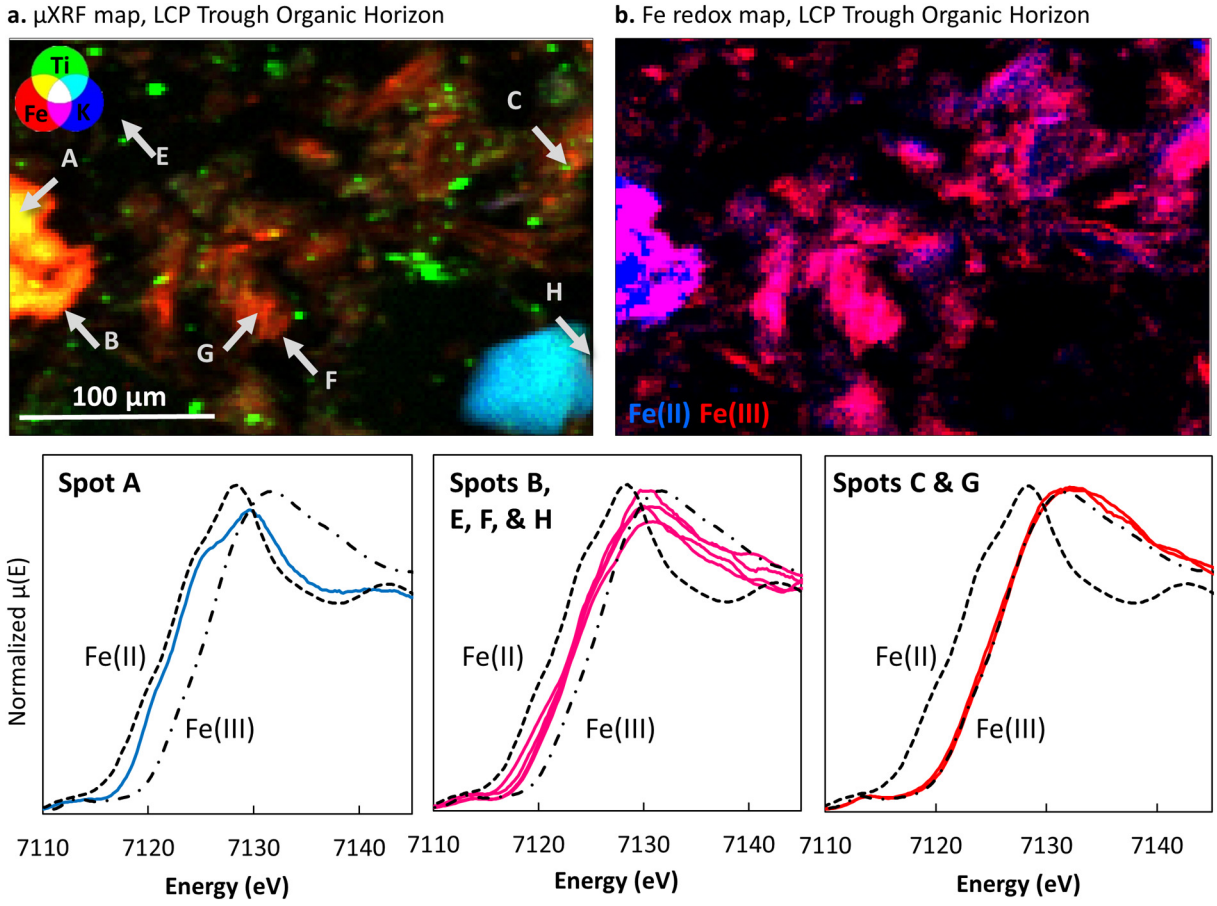

Fig. 5. (a) Micro-X-ray fluorescence map collected on a thin section of organic soil from the low-centered polygon trough showing spatial distribution of fluorescence intensity for Fe (red), Ti (green), and K (blue). (b) Fe redox map showing the spatial distribution of Fe(II) and Fe (III) for the area in panel (a). Individual μXANES spectra for spots c through i, marked by arrows in panel (a), are plotted as solid lines with standards for Fe(III) (ferrihydrite) and Fe(II) (FeO) plotted as dashed lines. Linear combination fits for these samples performed with nine single valence spectra are reported in Table 4. (For interpretation of the references to colour in this figure legend, the reader is referred to the web version of this article.)

interfaces and generate organo-Fe colloids that can be transported from tundra soils into river systems (Pokrovsky and Schott, 2002; Pokrovsky et al., 2006; Ilina et al., 2013). Although poorly crystalline and crystalline iron oxides dominated extractable Fe in all soils, organic-bound Fe, quantified as Fe released during organic matter oxidation, constituted up to 24% of Fe in some mineral soils (Table 1). Diffuse Fe coatings contained a mixture of Fe(III) and Fe(II) (Fig. 5) that likely included organic-Fe (III) and organic-Fe(II) complexes. Although it was clear that Fe was spatially associated with organic material (Fig. 4e and f), μXANES could not be used to differentiate between poorly crystalline Fe(III)-oxyhydroxides associated with organic matter and organic-bound Fe(III) species. Regions of mixed-valence, low-intensity Fe shown in Fig. 5 yielded weak diffraction patterns that were consistent with non-crystalline materials and could include organic-bound Fe species (Fig. 6).

Less than 20% of extractable Fe was present as exchangeable (Fe_{exch}), oxalate-extractable (Fe_{mag}), or oxidizable (Fe_{org}) iron species. Exchangeable Fe, though low in these recently-frozen soils, can increase rapidly during anoxic incubations due to microbial Fe-reduction (Roy Chowdhury et al., 2015). The precise nature of Fe_{mag} and Fe_{org} are hard to define solely using sequential extractions. Oxalate, used here to dissolve magnetite, may have also extracted metals from humic complexes and Fe-bearing minerals such as ilmenite (McKeague, 1967; Siregar et al., 2005). Although the presence of magnetite has previously been reported for soils in the BEO (Lipson et al., 2010) and is a known product of dissimilatory iron reduction (Lovley, 1991; Weber et al., 2006), its presence was not confirmed in these soils by μXRD or μXANES. Removal of Fe from humic-like complexes during oxalate extraction would consequently result in the underestimation of organic-bound Fe during peroxide extraction. Although Fe_{org} may also represent other oxidizable species, namely iron sulfides, their contribution to the Fe_{org} pool was likely relatively low given the sporadic detection of iron sulfides (Fig. 4j).

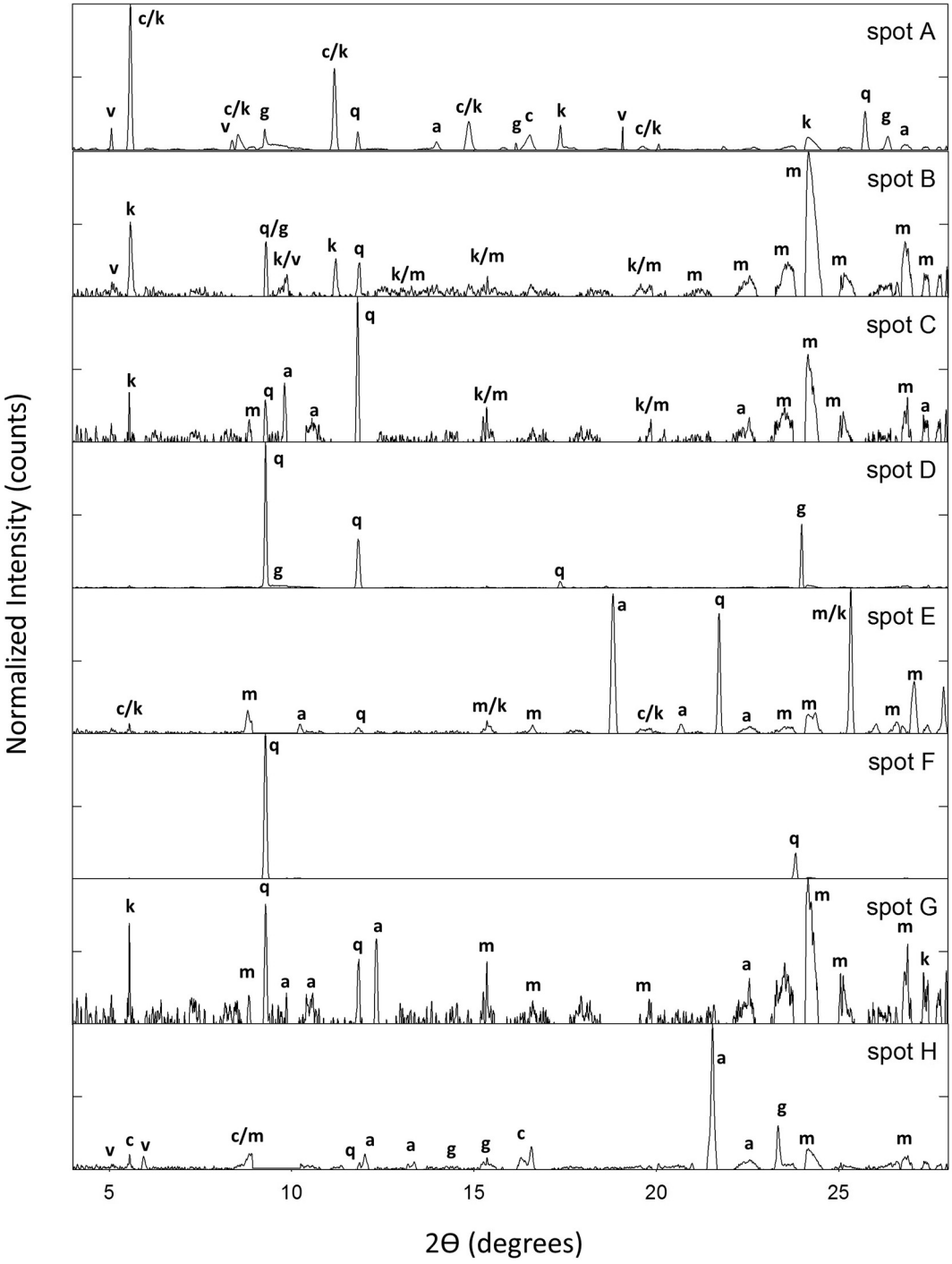

Fig. 6. Background-subtracted μXRD patterns acquired from organic horizon of the low-centered polygon trough for spots identified in Fig. 5a. Letters indicate peaks attributed to quartz (q), anorthite (a), chlorite (c), goethite (g), kaolinite (k), muscovite (m), and vivianite (v).

The presence of Fe(II)-bearing minerals indicates the potential for Fe to be sequestered following reductive dissolution of Fe(III)-oxyhydroxides. The Fe-sulfide minerals pyrite and greigite were identified in the mineral horizon of the low-centered polygon trough (Fig. 4j). Trough soils remain persistently saturated and anoxic at depth, conditions which promote Fe(III) and sulfate reduction followed by precipitation of iron sulfides (Lovley, 1991). Vivianite, a ferrous iron phosphate, was identified in close association with hematite and goethite in the organic horizon of the low-centered polygon trough (Figs. 5 and 6). Vivianite is often found in waterlogged soils with high concentrations of Fe(II) and PO_4^{3-} but low S^{2-} (Rothe et al., 2016). Co-localization of vivanite with goethite in soils, e.g., spot A

Table 4
Iron valence states for spots in Fig. 5 determined by linear combination fits.

Spot	Fe/I_0	Fe(II) (%)	Fe(III) (%)	Average valence	Reduced χ^2
Spot A	11.2	82	18	2.2	1.1×10^{-3}
Spot B	4.1	43	57	2.6	4.9×10^{-4}
Spot C	1.2	12	88	2.9	1.5×10^{-3}
Spot E	0.23	53	47	2.5	8.7×10^{-5}
Spot F	0.04	50	50	2.5	3.0×10^{-4}
Spot G	1.7	6	94	2.9	1.7×10^{-3}
Spot H	0.54	45	55	2.5	8.9×10^{-4}

in Fig. 5a, has been attributed to vivanite precipitation following microbial reduction of goethite during anoxic conditions (Heiberg et al., 2012; Walpersdorf et al., 2013). The presence of vivanite in the organic horizon but iron sulfides in the mineral horizon of the low-centered trough may indicate vertical stratification of Fe(II)-bearing phases. That is, sulfide precipitation dominates in the deeper, highly-anoxic soils whereas vivianite formation is limited to organic soils where sulfide is low but dissolved PO_4^{3-} is more abundant (Newman et al., 2015; Herndon et al., 2015a). Although Fe sulfides and phosphates were detected infrequently using microscale techniques and are likely only minor constituents, these minerals may exert strong controls on biogeochemical processes. For example, iron sulfides are expected to undergo rapid dissolution upon exposure to oxygen during dry periods when the water table drops and anoxic sediments are exposed to air. Vivianite may represent an important sink for the nutrient phosphate that is released into pore waters through decomposition of organic matter (Dijkstra et al., 2016). Therefore, the contribution of secondary Fe(II) phases to Fe cycling in Arctic peatlands should be further evaluated.

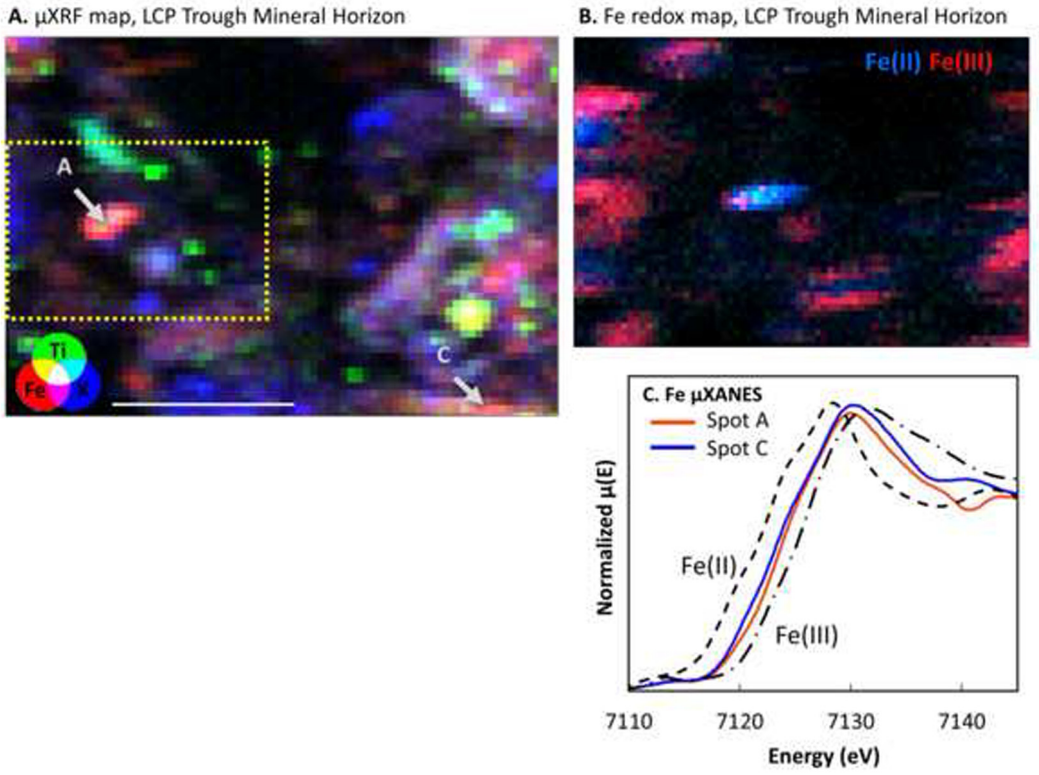

Fig. 7. (a) Micro-X-ray fluorescence map collected on a thin section of mineral soil from the low-centered polygon trough showing relative spatial intensities for Fe (red), Ti (green), and K (blue). (b) Fe redox map showing the spatial distribution of Fe(II) and Fe(III) for the area marked by a box in panel (a). Individual µXANES spectra for spots A and C, indicated by arrows in panel (a), are plotted as solid lines with standards for Fe(III) (ferrihydrite) and Fe(II) (FeO) plotted as dashed lines. XRD patterns for these spots are provided in Fig. A6. (For interpretation of the references to colour in this figure legend, the reader is referred to the web version of this article.)

4.2. Iron mobilization within the active layer

The relatively high quantities of poorly crystalline and crystalline iron oxide minerals in the organic horizon are consistent with a scenario where Fe-reduction in deep mineral soils produces dissolved Fe(II) that migrates upward in the soil profile and precipitates as ferrihydrite near the oxic-anoxic interface. Geochemical gradients in soil pore waters for these polygons support this conclusion. Concentrations of dissolved Fe(II) are enriched in pore waters deep in the mineral soil and decrease toward the soil surface, while dissolved Fe(III) peaks near the boundary between organic and mineral horizons, suggesting a zone of active oxidation that generates the observed iron oxides precipitates (Herndon et al., 2015a).

We previously reported that total concentrations of Fe and the ratios of Fe to relatively immobile elements Ti and Si were higher in organic horizons than in mineral horizons for low-centered polygon soils, indicating that Fe enrichment cannot be fully explained by simple physical mixing or cryoturbation of mineral particles into the organic horizon. Here, we determined using mass balance that $59 \pm 43\%$ of Fe in the organic horizon exceeds what can be explained by particle transport from the organic horizon. This "excess" Fe presumably derives from upward translocation of dissolved Fe(II) and Fe(III) and subsequent precipitation of oxidized Fe(III), and is similar to the proportion of Fe present as poorly crystalline oxides in organic horizons ($60 \pm 4\%$). The specific depth of solid-phase Fe accumulation could not be determined in this study because soils were homogenized over the entire thickness of each horizon; however, geochemical analyses over finer depth intervals could reveal the presence of a defined enrichment layer. Fiedler et al. (2004) similarly attributed Fe enrichment in low-centered polygons to solute migration along redox gradients, i.e., Fe diffused from anoxic, depressed regions to oxic, elevated regions and was immobilized along the oxidative barrier.

Enrichment of oxidized Fe in the organic horizon may both stabilize organic molecules, as discussed in the following section, and enhance decomposition of organic matter through microbial and abiotic processes. Indeed, Lipson et al. (2010, 2013) and Roy Chowdhury et al. (2015) concluded that Fe reduction contributes substantially to anaerobic respiration in drained thaw lake basins (DTLB) and interstitial polygonal ground in the Barrow Environmental Observatory. Ferrous iron oxidation can also produce hydroxyl radicals that abiotically oxidize organic molecules at redox interfaces to produce organic acids and CO_2 (Page et al., 2013). Herndon et al. (2015a, 2015b) observed positive correlations between dissolved Fe, methane, and organic acids such as acetate in both anaerobic soil incubations and in soil pore waters, concluding that Fe-reduction is concurrent with fermentation/methanogenesis and may even facilitate methane production by generating labile substrates through the oxidation of complex organic compounds (Kato et al., 2012; Zhuang et al., 2015). Subsequent incubation experiments by Yang et al. (2016) confirmed that Fe-reduction in anoxic soils from Barrow was associated with both oxidation of complex organic molecules and concurrent acetoclastic methanogenesis. The relative importance of Fe in increasing substrate decomposition through anaerobic respiration versus decreasing substrate accessibility in soils remains unresolved.

4.3. Mineral-associated organic carbon

Total organic carbon pools in the active layer (34 ± 3 kg C m^{-2}) were similar to the average SOC content (32 ± 27 kg m^{-2}) reported for the entire top 100 cm of Turbel soils in the circumpolar region (Tarnocai et al., 2009). Organic horizons contained variable concentrations of mineral-associated C that positively correlated with mineral content (Fig. 2). Indeed, we determined that $63 \pm 19\%$ of organic C in the active layer was associated with minerals, including $30 \pm 17\%$ of organic C in organic horizons. Our results indicate that the organic-rich soils in the active layer of Arctic tundra contain high proportions of mineral-associated carbon which could potentially slow degradation rates due to spatial isolation or interactions with mineral surface (Kögel-Knabner et al., 2008). Mueller et al. (2015) recently concluded that mineral-associated organic C was a minor component of SOC relative to particulate organic carbon (60% of SOC) in nearby drained-thaw lake basins; however, this discrepancy is possibly explained by their inclusion of upper permafrost layers which contain high concentrations of particulate C in buried organic horizons.

Iron may stabilize large quantities of mineral-associated organic matter through aggregation (Wiseman and Püttmann, 2006), coagulation (Wagai and Mayer, 2007; Riedel et al., 2012), and co-precipitation reactions (Cismasu et al., 2016). Here, we define aggregation as the stable clustering of organic particles with minerals such as iron oxides and clays, coagulation as the precipitation of organically-complexed metal cations, and co-precipitation as the incorporation of organic molecules into a mineral structure during mineral formation. Although it is difficult to differentiate between these associations in soils, it is likely that all of these processes contributed to stabilization of organic matter in tundra active layer. Iron, primarily as poorly crystalline oxyhydroxides, was present as diffuse coatings on particulate organic matter and minerals (e.g., Figs. 5 and 7), as discrete particles aggregated with clays and organic matter (e.g., Fig. 4l), and as thick precipitates around plant cells (e.g., Fig. 4e). Similar accumulations of Fe oxides around plant residues, recently observed in drained thaw lake basins, were found to both directly bind organic matter and facilitate formation of OM-stabilizing microaggregates (Mueller et al., 2017). Given that associations with poorly crystalline oxides stabilize organic matter and increase its residence time in soils (Torn et al., 1997; Kleber et al., 2005) the abundance of poorly crystalline oxide phases that we document here may serve a poorly understood role in increasing carbon storage in the Arctic tundra. Redox interfaces may be particularly important zones for carbon sequestration because organic molecules can coagulate with iron hydroxides during precipitation (Riedel et al., 2012), a process that preferentially sequesters aromatic compounds (e.g., plant biomolecules) and

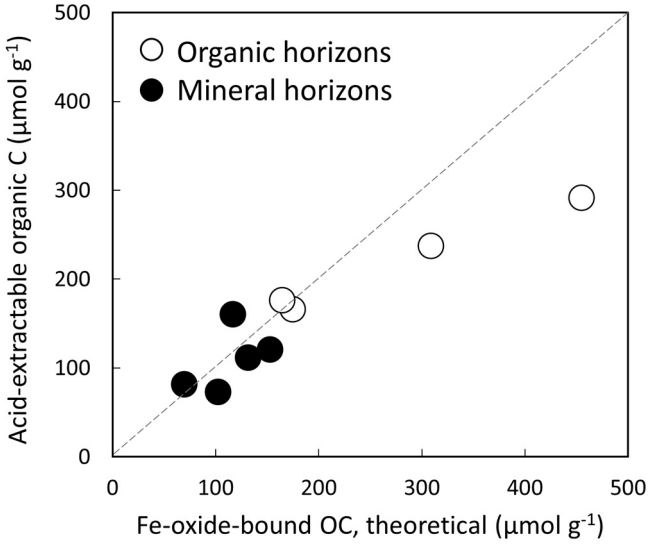

Fig. 8. Concentrations of acid-extractable organic carbon (μmol C g^{-1} soil) plotted versus the theoretical maximum adsorption of organic carbon to iron oxide surfaces, calculated as 3.22× the mass fraction of extractable Fe (g Fe g^{-1} soil) and converted to molar concentration (μmol C g^{-1} soil), following Kaiser et al. (1997) and Wagai and Mayer (2007).

enriches soil solution in carboxyl-rich molecules (Chorover and Amistadi, 2001; Christl and Kretzschmar, 2007; Riedel et al., 2012). Indeed, slight decreases in oxygen-containing functional groups (O—H and C═O) relative to aromatic-C in the high-density fraction may indicate preferential immobilization of aromatic compounds by iron oxide minerals (Fig. A3).

Iron oxide surfaces also temporarily sequester labile organic compounds through sorption reactions (Gu et al., 1994, 1995). Here, acid-extractable organic carbon (AEOC) largely represents organic molecules liberated through proton-promoted dissolution of iron oxides (Wiederhold et al., 2006). AEOC was chemically similar to water-extractable organic C but distinct from other extracted pools of organic matter (Fig. 3a and b). WEOC and AEOC were dominated by hydroxyl functional groups with lesser contributions from polysaccharide-C, aromatic-C, carboxylate-C and aliphatic-C, consistent with a mixture of alcohols, sugars, and small molecular weight organic acid and aromatic compounds that are released through decomposition of larger molecules and subsequently converted to organic acids, CO_2, and CH_4 (Herndon et al., 2015b; Yang et al., 2016). We propose that labile organic molecules are exchanged between WEOC and AEOC fractions primarily through adsorption to and desorption from iron oxide surfaces over short time scales.

The potential for Fe-oxides to bind organic compounds through sorption was evaluated using an empirical relationship reported by Kaiser et al. (1997) that Fe oxyhydroxides can sorb up to 0.22 g OC g Fe^{-1} (e.g., Wagai and Mayer, 2007). The theoretical quantity of adsorbed organic C (g OC g $soil^{-1}$) was calculated as 0.22× extractable Fe (g Fe g $soil^{-1}$) for each soil and converted to molar concentration (μmol OC g $soil^{-1}$). Concentrations of acid-extractable organic C were highly similar to theoretical values for organic C adsorption to Fe-oxides (Fig. 8), suggesting that the surface area provided by iron oxides in these soils is sufficient to explain the pool of acid-extractable organic C. Inner-sphere complexes between iron oxides and organic matter, primarily through carboxylate functional groups, are favored under these acidic (pH ∼ 4.5–6.3) and organic-rich conditions (Kleber et al., 2015). We infer that organic compounds occupied all available sorption sites on iron oxyhydroxides with the exception of soils with especially high Fe concentrations. AEOC values that were slightly above the theoretical sorption capacity are potentially attributed to release of organic molecules bound to aluminum hydroxide mineral surfaces (Kleber et al., 2005). Thus, sorption of water-soluble organic molecules to Fe-oxyhydroxide and possibly other metal hydroxide surfaces may limit the solubility of a small (<2% of SOC) but readily-degradable pool of low-molecular weight organic compounds.

5. CONCLUSIONS

Our study demonstrates that Fe and organic C exhibit close spatial relationships in the seasonally thawed active layer, which suggests a potential for Fe to stabilize organic carbon and increase its residence time in Arctic soils. Dynamic Fe redox cycling is driven by vertical redox gradients induced by persistent soil saturation. This work also characterizes the forms of Fe(III) available to anaerobic iron-reducing bacteria throughout the soil column. Dissolved Fe(II) that is released during Fe(III)-reduction deep in the mineral soil is either sequestered in secondary Fe(II)-phases (i.e., pyrite, vivanite) or migrates upwards and is oxidized at the anoxic–oxic interface in the organic horizon. Continued upward translocation and oxidation of Fe has enriched organic horizons in poorly-crystalline and crystalline iron oxides that are co-mingled with organic matter

and mineral grains. Iron enrichment at the redox interface may hinder degradation of organic matter through multiple mechanisms that include adsorption of water-soluble organic molecules to iron oxide surfaces, aggregation of particulate organic matter with iron oxides and clays, and coagulation of insoluble Fe(II) and Fe(III) organic complexes. In some cases, thick iron oxide coatings on plant debris form barriers that may inhibit microbial access to particulate organic carbon. However, the relative importance of Fe in limiting decomposition via mineral-stabilization versus promoting decomposition through anaerobic respiration remains unresolved.

It is critical to understand geochemical processes in Arctic and subarctic systems given that ongoing changes in soil temperature and hydrology will impact redox conditions and rates of organic matter decomposition (Hinzman et al., 2013). Currently, abiotic controls on biological processes (e.g., C cycles, nutrient fluxes, greenhouse gas production) are poorly understood for these systems. Soil moisture and wetland extent are expected to decrease in many areas of the Arctic (Hinzman et al., 2013) a process that could facilitate further precipitation of iron oxide minerals currently limited by cold temperatures, persistent water saturation, and organic-complexation of dissolved Fe(III) (Karlsson and Persson, 2010; Sundman et al., 2014). The implication of this result is that dissolved and organic-bound Fe(II) and Fe(III) will precipitate as iron oxide minerals under warmer, drier conditions due to decreased anoxia and increased decomposition of organic matter. These complex dynamics between Fe and organic matter are important to study given that mineral-protection may influence decomposition of organic matter and determine whether terrestrial ecosystems act as future sinks or sources of carbon.

ACKNOWLEDGEMENTS

We gratefully acknowledge Stan Wullschleger, Bob Busey, Larry Hinzman, Kenneth Lowe and Craig Ulrich for obtaining and analyzing frozen core samples, Carla Rosenfeld and Lauren Kinsman-Costello for assistance with statistical analyses, Ziming Yang for assisting at the beamline, and Deanne Brice for soil carbon and nitrogen analysis, as well as logistical support in Barrow provided by UIC Science, LLC. Three anonymous reviewers are acknowledged for their comments to improve the manuscript. The Next-Generation Ecosystem Experiments (NGEE Arctic) project is supported by the Office of Biological and Environmental Research in the U.S. Department of Energy (DOE) Office of Science. Oak Ridge National Laboratory is managed by UT-Battelle LLC, for the DOE under Contract No. DE-AC05-00OR22725. All data are available in the supporting information for this manuscript and in an online data repository (NGEE-Arctic Data Portal). Support for A.B.A. was provided by National Science Foundation (NSF) – Division of Biological Infrastructure award (DBI-1263263 to M. Kershner). This research used resources of the Advanced Photon Source, a DOE Office of Science User Facility operated by Argonne National Laboratory under Contract No. DE-AC02-06CH11357. We acknowledge the support of GeoSoilEnviroCARS (Sector 13), which is supported by NSF Earth Sciences (EAR-1128799), and DOE Geosciences (DE-FG02-94ER14466).

APPENDIX A. SUPPLEMENTARY MATERIAL

Supplementary data associated with this article can be found, in the online version, at http://dx.doi.org/10.1016/j.gca.2017.02.034.

REFERENCES

Amacher M. C., Henderson R. E., Breithaupt M. D., Seale C. L. and LaBauve J. M. (1990) Unbuffered and buffered salt methods for exchangeable cations and effective cation-exchange capacity. *Soil Sci. Soc. Am. J.* **54**(4), 1036–1042.

Amstaetter K., Borch T. and Kappler A. (2012) Influence of humic acid imposed changes of ferrihydrite aggregation on microbial Fe(III) reduction. *Geochim. Cosmochim. Acta* **85**, 326–341. http://dx.doi.org/10.1016/j.gca.2012.02.003.

Baldock J. A. and Skjemstad J. O. (2000) Role of the soil matrix and minerals in protecting natural organic materials against biological attack. *Org. Geochem.* **31**, 697–710.

Benjamini Y. and Hochberg Y. (1995) Controlling the false discovery rate: a practical and powerful approach to multiple testing. *J. R. Stat. Soc. Series B Stat. Methodol.*, 289–300.

Bjerrum C. and Canfield D. (2002) Ocean productivity before about 1.9 Gyr ago limited by phosphorus adsorption onto iron oxides. *Nature* **417**(6885), 159–162.

Bockheim J. G., Hinkel K. M. and Nelson F. E. (2001) Soils of the Barrow region, Alaska. *Polar Geogr.* **25**(3), 163–181.

Bockheim J. G., Hinkel K. M. and Nelson F. E. (2003) Predicting carbon storage in tundra soils of Arctic Alaska. *Soil Sci. Soc. Am. J.* **67**(3), 948. http://dx.doi.org/10.2136/sssaj2003.0948.

Borch T., Kretzschmar R., Skappler A., Van Cappellen P., Ginder-Vogel M., Voegelin A. and Campbell K. (2010) Biogeochemical redox processes and their impact on contaminant dynamics. *Environ. Sci. Technol.* **44**(1), 15–23. http://dx.doi.org/10.1021/es9026248.

Borggaard O. K., Jorgensen S. S., Moberg J. P. and Raben-Lange B. (1990) Influence of organic matter on phosphate adsorption by aluminium and iron oxides in sandy soils. *J. Soil Sci.* **41**(3), 443–449.

Boyer J. N. and Groffman P. M. (1996) Bioavailability of water extractable organic carbon fractions in forest and agricultural soil profiles. *Soil Biol. Biochem.* **28**(6), 783–790. http://dx.doi.org/10.1016/0038-0717(96), 00015-6.

Brimhall G. H. and Dietrich W. E. (1987) Constitutive mass balance relations between chemical composition, volume, density, porosity, and strain in metasomatic hydrochemical systems: results on weathering and pedogenesis. *Geochim. Cosmochim. Acta* **51**(3), 567–587.

Brown J., Everett K. R., Webber P. J., MacLean S. F. and Murray D. F. (1980) The coastal tundra at Barrow. In *An Arctic Ecosystem: The Coastal Tundra at Barrow, Alaska*, pp. 1–29. http://dx.doi.org/10.1575/1912/222.

Chorover J. and Amistadi M. K. (2001) Reaction of forest floor organic matter at goethite, birnessite and smectite surfaces. *Geochim. Cosmochim. Acta* **65**(1), 95–109. http://dx.doi.org/10.1016/S0016-7037(00), 00511-1.

Chowdhury T. and Graham D. (2013) Soil Physicochemical Characteristics from Ice Wedge Polygons, Barrow, Alaska, Ver. 1.. *Next Generation Ecosystems Experiment-Arctic*. Oak Ridge National Laboratory (ORNL), Oak Ridge, TN (US). http://dx.doi.org/10.5440/1109232.

Christl I. and Kretzschmar R. (2007) C-1s NEXAFS spectroscopy reveals chemical fractionation of humic acid by cation-induced coagulation. *Environ. Sci. Technol.* **41**(6), 1915–1920.

Cismasu A. C., Michel F. M., Tcaciuc A. P., Tyliszczak T. and Brown, Jr, G. E. (2011) Composition and structural aspects of naturally occurring ferrihydrite. *C. R. Geosci.* **343**(2), 210–218.

Cismasu A. C., Williams K. H. and Nico P. S. (2016) Iron and carbon dynamics during aging and reductive transformation of biogenic ferrihydrite. *Environ. Sci. Technol.* **50**(1), 25–35. http://dx.doi.org/10.1021/acs.est.5b03021.

Crow S. E., Swanston C. W., Lajtha K., Brooks J. R. and Keirstead H. (2007) Density fractionation of forest soils: methodological questions and interpretation of incubation results and turnover time in an ecosystem context. *Biogeochemistry* **85**(1), 69–90. http://dx.doi.org/10.1007/s10533-007-9100-8.

Davidson E. A. and Janssens I. A. (2006) Temperature sensitivity of soil carbon decomposition and feedbacks to climate change. *Nature* **440**, 165–173. http://dx.doi.org/10.1038/nature04514.

Dijkstra N., Slomp C. P. and Behrends T. (2016) Vivianite is a key sink for phosphorus in sediments of the Landsort Deep, an intermittently anoxic deep basin in the Baltic Sea. *Chem. Geol.* **438**, 58–72. http://dx.doi.org/10.1016/j.chemgeo.2016.05.025.

Elberling B., Michelsen A., Schädel C., Schuur E. A. G., Christiansen H. H., Berg L. and Ellipsis Sigsgaard C. (2013) Long-term CO_2 production following permafrost thaw. *Nat. Clim. Change* **3**, 890–894. http://dx.doi.org/10.1038/nclimate1955.

Emerson D., Emerson D., Scott J. J., Benes J. and Bowden B. (2015) Microbial iron oxidation in the Arctic tundra and the implications for biogeochemical cycling. *Appl. Environ. Microbiol.* **81**, 8066–8075. http://dx.doi.org/10.1128/AEM.02832-15.

Emerson D., Weiss J. V. and Megonigal J. P. (1999) Iron-oxidizing bacteria are associated with ferric hydroxide precipitates (Fe-plaque) on the roots of wetland plants. *Appl. Environ. Microbiol.* **65**(6), 2758–2761.

Fiedler S., Wagner D., Kutzbach L. and Pfeiffer E.-M. (2004) Element redistribution along hydraulic and redox gradients of low-centered polygons, Lena Delta, Northern Siberia. *Soil Sci. Soc. Am. J.* **68**(3), 1002. http://dx.doi.org/10.2136/sssaj2004.1002.

Gu B., Schmitt J., Chen Z., Liang L. and McCarthy J. F. (1994) Adsorption and desorption of natural organic matter on iron oxide: mechanisms and models. *Environ. Sci. Technol.* **28**(1), 38–46. http://dx.doi.org/10.1021/es00050a007.

Gu B., Schmitt J., Chen Z., Liang L. and McCarthy J. F. (1995) Adsorption and desorption of different organic matter fractions on iron oxide. *Geochim. Cosmochim. Acta* **59**(2), 219–229.

Hall S. J. and Silver W. L. (2013) Iron oxidation stimulates organic matter decomposition in humid tropical forest soils. *Global Change Biol.* **19**(9), 2804–2813. http://dx.doi.org/10.1111/gcb.12229.

Hansel C. M., Fendorf S., Sutton S. and Newville M. (2001) Characterization of Fe plaque and associated metals on the roots of mine-waste impacted aquatic plants. *Environ. Sci. Technol.* **35**(19), 3863–3868. http://dx.doi.org/10.1021/es0105459.

Hay M. B. and Myneni S. C. (2007) Structural environments of carboxyl groups in natural organic molecules from terrestrial systems. Part 1: infrared spectroscopy. *Geochim. Cosmochim. Acta* **71**(14), 3518–3532.

Heiberg L., Koch C. B., Kjaergaard C., Jensen H. S. and Hans Christian B. H. (2012) Vivianite precipitation and phosphate sorption following iron reduction in anoxic soils. *J. Environ. Qual.* **41**(3), 938–949. http://dx.doi.org/10.2134/jeq2011.0067.

Herndon E. M., Yang Z., Bargar J., Janot N., Regier T. Z., Graham D. E., Gu B. and Liang L. (2015a) Geochemical drivers of organic matter decomposition in arctic tundra soils. *Biogeochemistry* **126**(3), 397–414. http://dx.doi.org/10.1007/s10533-015-0165-5.

Herndon E. M., Mann B. F., Roy Chowdhury T., Yang Z., Wullschleger S. D., Graham D., Liang L. and Gu B. (2015b) Pathways of anaerobic organic matter decomposition in tundra soils from Barrow, Alaska. *J. Geophys. Res. Biogeosci.* **120**(11), 2345–2359. http://dx.doi.org/10.1002/2015JG003147.

Hinzman L. D., Deal C. J., Mcguire A. D., Mernild S. H., Polyakov I. V. and Walsh J. E. (2013) Trajectory of the Arctic as an integrated system. *Ecol. Appl.* **23**(8), 1837–1868. http://dx.doi.org/10.1890/11-1498.1.

Hishi T., Hirobe M., Tateno R. and Takeda H. (2004) Spatial and temporal patterns of water-extractable organic carbon (WEOC) of surface mineral soil in a cool temperate forest ecosystem. *Soil Biol. Biochem.* **36**(11), 1731–1737. http://dx.doi.org/10.1016/j.soilbio.2004.04.030.

Hobara S., Koba K., Ae N., Giblin A. E., Kushida K. and Shaver G. R. (2013) Geochemical influences on solubility of soil organic carbon in arctic tundra ecosystems. *Soil Sci. Soc. Am. J.* **77**(2), 473. http://dx.doi.org/10.2136/sssaj2012.0199.

Hubbard S. S., Gangodagamage C., Dafflon B., Wainwright H., Peterson J., Gusmeroli A., Ulrich C., Wu Y., Wilson C., Rowland J., Tweedie C. and Wullschleger S. D. (2013) Quantifying and relating land-surface and subsurface variability in permafrost environments using LiDAR and surface geophysical datasets. *Hydrogeol. J.* **21**(1), 149–169. http://dx.doi.org/10.1007/s10040-012-0939-y.

Huemmrich K. F., Kinoshita G., Gamon J. a., Houston S., Kwon H. and Oechel W. C. (2010) Tundra carbon balance under varying temperature and moisture regimes. *J. Geophys. Res.* **115**, 1–8. http://dx.doi.org/10.1029/2009JG001237.

Hugelius G., Strauss J., Zubrzycki S., Harden J. W., Schuur E. A. G., Ping C. L., Schirrmeister L., Grosse G., Michaelson G. J., Koven C. D., O'Donnell J. A., Elberling B., Mishra U., Camill P., Yu Z., Palmtag J. and Kuhry P. (2014) Estimated stocks of circumpolar permafrost carbon with quantified uncertainty ranges and identified data gaps. *Biogeosciences* **11**(23), 6573–6593. http://dx.doi.org/10.5194/bg-11-6573-2014.

Ilina S. M., Poitrasson F., Lapitskiy S. A., Alekhin Y. V., Viers J. and Pokrovsky O. S. (2013) Extreme iron isotope fractionation between colloids and particles of boreal and temperate organic-rich waters. *Geochim. Cosmochim. Acta* **101**, 96–111. http://dx.doi.org/10.1016/j.gca.2012.10.023.

Iversen C., Vander Stel H., Norby R., Sloan V., Childs J., Brice D., Keller J., Jong A., Ladd M. and Wullschleger S. (2012). Active Layer Soil Carbon and Nutrient Mineralization, Barrow, Alaska, 2012.

Jandl R. and Sollins P. (1997) Water-extractable soil carbon in relation to the belowground carbon cycle. *Biol. Fertil. Soils* **25**(2), 196–201. http://dx.doi.org/10.1007/s003740050303.

Jensen H. S., Kristensen P., Jeppesen E. and Skytthe A. (1992) Iron:phosphorus ratio in surface sediment as an indicator of phosphate release from aerobic sediments in shallow lakes. *Hydrobiologia* **235/236**(1), 731–743. http://dx.doi.org/10.1007/BF00026261.

Jorgenson M. T., Shur Y. L. and Pullman E. R. (2006) Abrupt increase in permafrost degradation in Arctic Alaska. *Geophys. Res. Lett.* **33**(2), 2–5. http://dx.doi.org/10.1029/2005GL024960.

Kaiser K., Guggenberger G., Haumaier L. and Zech W. (1997) Dissolved organic matter sorption on sub soils and minerals studied by 13C-NMR and DRIFT spectroscopy. *Eur. J. Soil Sci.* **48**(2), 301–310.

Kaiser C., Meyer H., Biasi C., Rusalimova O., Barsukov P. and Richter A. (2007) Conservation of soil organic matter through cryoturbation in arctic soils in Siberia. *J. Geophys. Res.*

Biogeosci. **112**(2), 1–8. http://dx.doi.org/10.1029/2006JG000258.

Karlsson T. and Persson P. (2010) Coordination chemistry and hydrolysis of Fe(III) in a peat humic acid studied by X-ray absorption spectroscopy. *Geochim. Cosmochim. Acta* **74**, 30–40. http://dx.doi.org/10.1016/j.gca.2009.09.023.

Karlsson T., Persson P., Skyllberg U., Mörth C.-M. and Giesler R. (2008) Characterization of iron(III) in organic soils using extended X-ray absorption fine structure spectroscopy. *Environ. Sci. Technol.* **42**(15), 5449–5454. http://dx.doi.org/10.1021/es800322j.

Kato S., Hashimoto K. and Watanabe K. (2012) Methanogenesis facilitated by electric syntrophy via (semi) conductive iron-oxide minerals. *Environ. Microbiol.* **14**(7), 1646–1654.

Kleber M., Eusterhues K., Keiluweit M., Mikutta C., Mikutta R. and Nico P. S. (2015) Mineral-organic associations: formation, properties, and relevance in soil environments. *Adv. Agron.* **130**, 1–140. http://dx.doi.org/10.1016/bs.agron.2014.10.005.

Kleber M., Mikutta R., Torn M. S. and Jahn R. (2005) Poorly crystalline mineral phases protect organic matter in acid subsoil horizons. *Eur. J. Soil Sci.* **56**(6), 717–725. http://dx.doi.org/10.1111/j.1365-2389.2005.00706.x.

Kögel-Knabner I., Guggenberger G., Kleber M., Kandeler E., Kalbitz K., Scheu S., Eusterhues K. and Leinweber P. (2008) Organo-mineral associations in temperate soils: Integrating biology, mineralogy, and organic matter chemistry. *J. Plant Nutr. Soil Sci.* **171**(1), 61–82.

Kraft S., Stümpel J., Becker P. and Kuetgens U. (1996) High resolution x-ray absorption spectroscopy with absolute energy calibration for the determination of absorption edge energies. *Rev. Sci. Instrum.* **67**(3), 681–687.

Lalonde K., Mucci A., Ouellet A. and Gelinas Y. (2012) Preservation of organic matter in sediments promoted by iron. *Nature* **483**, 198–200. http://dx.doi.org/10.1038/nature10855.

Lehmann J. and Kleber M. (2015) The contentious nature of soil organic matter. *Nature* **528**(7580), 60–68. http://dx.doi.org/10.1038/nature16069.

Lipson D. A., Jha M., Raab T. K. and Oechel W. C. (2010) Reduction of iron (III) and humic substances plays a major role in anaerobic respiration in an Arctic peat soil. *J. Geophys. Res. Biogeosci.* **115**(4), 1–13. http://dx.doi.org/10.1029/2009JG001147.

Lipson D. A., Raab T. K., Goria D. and Zlamal J. (2013) The contribution of Fe(III) and humic acid reduction to ecosystem respiration in drained thaw lake basins of the Arctic Coastal Plain. *Global Biogeochem. Cycl.* **27**(2), 399–409. http://dx.doi.org/10.1002/gbc.20038.

Lipson D. A., Zona D., Raab T. K., Bozzolo F., Mauritz M. and Oechel W. C. (2012) Water-table height and microtopography control biogeochemical cycling in an Arctic coastal tundra ecosystem. *Biogeosciences* **9**(1), 577–591. http://dx.doi.org/10.5194/bg-9-577-2012.

Lovely D. and Phillips E. (1986) Organic matter mineralization with reduction of ferric iron in anaerobic sediments. *Appl. Environ. Microbiol.* **51**, 683–689.

Lovley D. R. (1991) Dissimilatory Fe (III) and Mn (IV) reduction. *Microbiol. Rev.* **55**(2), 259–287.

Lovley D. R., Stolz J. F., Nord G. L. and Phillips E. J. P. (1987) Anaerobic production of magnetite by a dissimilatory iron-reducing microorganism. *Nature* **330**(6145), 252–254. http://dx.doi.org/10.1038/330252a0.

Lutzow M. V., Knogel-Knabner I., Ekschmitt K., Matzner E., Guggenberger G., Marschner B. and Flessa H. (2006) Stabilization of organic matter in temperate soils: Mechanisms and their relevance under different soil conditions – a review. *Eur. J. Soil Sci.* **57**(4), 426–445. http://dx.doi.org/10.1111/j.1365-2389.2006.00809.x.

McKeague J. (1967) An evaluation of 0.1 M pyrophosphate and pyrophosphate-dithionite in comparison with oxalate as extractants of the accumulation products in podzols and some other soils. *Can. J. Soil Sci.* **47**, 95–99.

Miller K. E., Lai C.-T., Friedman E. S., Angenent L. T. and Lipson D. a. (2015) Methane suppression by iron and humic acids in soils of the Arctic Coastal Plain. *Soil Biol. Biochem.* **83**, 176–183. http://dx.doi.org/10.1016/j.soilbio.2015.01.022.

Mueller C. W., Rethemeyer J., Kao-Kniffin J., Löppmann S., Hinkel K. M. and Bockheim J. G. (2015) Large amounts of labile organic carbon in permafrost soils of northern Alaska. *Global Change Biol.* **21**(7), 2804–2817. http://dx.doi.org/10.1111/gcb.12876.

Mueller C. W., Hoeschen C., Steffens M., Buddenbaum H., Hinkel K., Bockheim J. G. and Kao-Kniffin J. (2017) Microscale soil structures foster organic matter stabilization in permafrost soils. *Geoderma* **293**, 44–53.

Neaman A., Chorover J. and Brantley S. L. (2006) Effects of organic ligands on granite dissolution in batch experiments at pH 6. *Am. J. Sci.* **306**(6), 451–473. http://dx.doi.org/10.2475/06.2006.03.

Newman B. D., Throckmorton H. M., Graham D. E., Gu B., Hubbard S. S., Liang L. and Ellipsis Wullschleger S. D. (2015) Microtopographic and depth controls on active layer chemistry in Arctic polygonal ground. *Geophys. Res. Lett.* **42**(6), 1808–1817. http://dx.doi.org/10.1002/2014GL062804.

Olefeldt D., Turetsky M. R., Crill P. M. and Mcguire A. D. (2013) Environmental and physical controls on northern terrestrial methane emissions across permafrost zones. *Global Change Biol.* **19**(2), 589–603. http://dx.doi.org/10.1111/gcb.12071.

Osterkamp T. E. and Romanovsky V. E. (1999) Evidence for warming and thawing of discontinuous permafrost in Alaska. *Permafrost Periglac.* **10**(1), 17–37.

Pachauri, R., Allen, M., Barros, V., Broome, J., Cramer, W., Christ, R., Church, J.A., Clarke, L., Dahe, Q., Dasgupta, P., and Dubash, N., 2014. Climate change 2014: synthesis report. *Contribution of working groups I, II and III to the fifth assessment report of the intergovernmental panel on climate change*.

Page S. E., Kling G. W., Sander M., Harrold K. H., Robert J., Mcneill K. and Cory R. M. (2013) Dark production of hydroxyl radical in arctic soil and surface waters. *Environ. Sci. Technol.* **47**, 12860–12867.

Pokrovsky O. S., Manasypov R. M., Loiko S. V. and Shirokova L. S. (2016) Organic and organo-mineral colloids in discontinuous permafrost zone. *Geochim. Cosmochim. Acta* **188**, 1–20. http://dx.doi.org/10.1016/j.gca.2016.05.035.

Pokrovsky O. S. and Schott J. (2002) Iron colloids/organic matter associated transport of major and trace elements in small boreal rivers and their estuaries (NW Russia). *Chem. Geol.* **190**(1–4), 141–179. http://dx.doi.org/10.1016/S0009-2541(02)00115-8.

Pokrovsky O. S., Schott J. and Dupré B. (2006) Trace element fractionation and transport in boreal rivers and soil porewaters of permafrost-dominated basaltic terrain in Central Siberia. *Geochim. Cosmochim. Acta* **70**(13), 3239–3260. http://dx.doi.org/10.1016/j.gca.2006.04.008.

Poulton S. W. and Canfield D. E. (2005) Development of a sequential extraction procedure for iron: implications for iron partitioning in continentally derived particulates. *Chem. Geol.* **214**(3–4), 209–221. http://dx.doi.org/10.1016/j.chemgeo.2004.09.003.

Prescher C. and Prakapenka V. B. (2015) DIOPTAS : a program for reduction of two-dimensional X-ray diffraction data and

data exploration. *High Press. Res.* **7959**, 1–8. http://dx.doi.org/10.1080/08957959.2015.1059835.

Pribyl D. W. (2010) A critical review of the conventional SOC to SOM conversion factor. *Geoderma* **156**(3), 75–83.

Prietzel J., Thieme J., Eusterhues K. and Eichert D. (2007) Iron speciation in soils and soil aggregates by synchrotron-based X-ray microspectroscopy (XANES, μ-XANES). *Eur. J. Soil Sci.* **58**(5), 1027–1041. http://dx.doi.org/10.1111/j.1365-2389.2006.00882.x.

Ravel B. and Newville M. (2005) ATHENA, ARTEMIS, HEPHAESTUS: data analysis for X-ray absorption spectroscopy using IFEFFIT. *J. Synchrotron Radiat.* **12**(4), 537–541.

Riedel T., Biester H. and Dittmar T. (2012) Molecular fractionation of dissolved organic matter with metal salts. *Environ. Sci. Technol.* **46**(8), 4419–4426. http://dx.doi.org/10.1021/es203901u.

Riordan B., Verbyla D. and McGuire A. D. (2006) Shrinking ponds in subarctic Alaska based on 1950–2002 remotely sensed images. *J. Geophys. Res. Biogeosci.* **111**(4). http://dx.doi.org/10.1029/2005JG000150.

Roden E. E. and Edmonds J. (1997) Phosphate mobilization in iron-rich anaerobic sediments: microbial Fe (III) oxide reduction versus iron-sulfide formation. *Arch. Hydrobiol.* **139**(3), 347–378.

Roden E. E. and Wetzel R. G. (1996) Organic carbon oxidation and suppression of methane production by microbial Fe(III) oxide reduction in vegetated and unvegetated freshwater wetland sediments. *Limnol. Oceanogr.* **41**(8), 1733–1748. http://dx.doi.org/10.4319/lo.1996.41.8.1733.

Rothe M., Kleeberg A. and Hupfer M. (2016) The occurrence, identification and environmental relevance of vivianite in waterlogged soils and aquatic sediments. *Earth-Sci. Rev.* **158**, 51–64. http://dx.doi.org/10.1016/j.earscirev.2016.04.008.

Roy Chowdhury T., Herndon E. M., Phelps T. J., Elias D., Gu B., Liang L., Wullschleger S. and Graham D. E. (2015) Stoichiometry and temperature sensitivity of methanogenesis and CO_2 production from saturated polygonal tundra in Barrow, Alaska. *Global Change Biol.* **21**, 722–737. http://dx.doi.org/10.1111/gcb.12762.

Ryan M. G., Melillo J. M. and Ricca A. (1990) A comparison of methods for determining proximate carbon fractions in forest litter. *Can. J. For. Res.* **20**, 166–171.

Schuur E. A. G., Vogel J. G., Crummer K. G., Lee H., Sickman J. O. and Osterkamp T. E. (2009) The effect of permafrost thaw on old carbon release and net carbon exchange from tundra. *Nature* **459**(7246), 556–559. http://dx.doi.org/10.1038/nature08031.

Schwertmann U. (2008) Iron oxides. In *Encyclopedia of Soil Science*. Springer, Netherlands, pp. 363–369.

Schwertmann U. and Murad E. (1988) The nature of an iron oxide-organic iron association in a peaty environment. *Clay Miner.* **23**(3), 291–299.

Schädel C., Bader M. K. F., Schuur E. A., Biasi C., Bracho R., Čapek P., De Baets S., Diakova K., Ernakovich J., Estop-Aragones C., Graham D. E., Hartley I. P., Iversen C. M., Kane E., Knoblauch C., Lupascu M., Martikainen P. J., Natali S., Norby R. J., O'Donnell J., Roy Chowdhury T., Santruckova H., Shaver G., Sloan V. L., Treat C. C., Turetsky M. R., Waldrop M. P. and Wickland K. P. (2016) Potential carbon emissions dominated by carbon dioxide from thawed permafrost soils. *Nat. Clim. Change* **6**, 950–953.

Siregar A., Kleber M., Mikutta R. and Jahn R. (2005) Sodium hypochlorite oxidation reduces soil organic matter concentrations without affecting inorganic soil constituents. *Eur. J. Soil Sci.* **56**(4), 481–490. http://dx.doi.org/10.1111/j.1365-2389.2004.00680.x.

Smith L. C., Sheng Y., MacDonald G. M. and Hinzman L. D. (2005) Disappearing Arctic lakes. *Science* **308**(5727), 1429. http://dx.doi.org/10.1126/science.1108142.

Solomon D., Lehmann J., Kinyangi J., Liang B. and Schafer T. (2005) Carbon K-Edge NEXAFS and FTIR-ATR spectroscopic investigation of organic carbon speciation in soils. *Soil Sci. Soc. Am. J.* **69**(1), 107–119. http://dx.doi.org/10.2136/sssaj2005.0107dup.

Sundman A., Karlsson T., Laudon H. and Persson P. (2014) XAS study of iron speciation in soils and waters from a boreal catchment. *Chem. Geol.* **364**, 93–102. http://dx.doi.org/10.1016/j.chemgeo.2013.11.023.

Swanston C. W., Torn M. S., Hanson P. J., Southon J. R., Garten C. T., Hanlon E. M. and Ganio L. (2005) Initial characterization of processes of soil carbon stabilization using forest stand-level radiocarbon enrichment. *Geoderma* **128**(1–2), 52–62. http://dx.doi.org/10.1016/j.geoderma.2004.12.015.

Tarnocai C., Canadell J. G., Schuur E. A. G., Kuhry P., Mazhitova G. and Zimov S. (2009) Soil organic carbon pools in the northern circumpolar permafrost region. *Global Biogeochem. Cycl.* **23**(2), 1–11. http://dx.doi.org/10.1029/2008GB003327.

Tessier A., Campbell P. G. C. and Bisson M. (1979) Sequential extraction procedure for the speciation of particulate trace metals. *Anal. Chem.* **51**(7), 844–851.

Theis T. L. and Singer P. C. (1974) Complexation of iron(II) by organic matter and its effect on iron(II) oxidation. *Environ. Sci. Technol.* **8**(6), 569–573. http://dx.doi.org/10.1021/es60091a008.

Thompson A., Chadwick O. A., Rancourt D. G. and Chorover J. (2006) Iron-oxide crystallinity increases during soil redox oscillations. *Geochim. Cosmochim. Acta* **70**(7), 1710–1727. http://dx.doi.org/10.1016/j.gca.2005.12.005.

Torn M. S., Trumbore S. E., Chadwick O. A., Vitousek P. M. and Hendricks D. M. (1997) Mineral control of soil organic carbon storage and turnover content were measured by horizon down to the depth at which. *Nature* **389**(1992), 3601–3603. http://dx.doi.org/10.1038/38260.

Turetsky M. R., Treat C. C., Waldrop M. P., Waddington J. M., Harden J. W. and McGuire A. D. (2008) Short-term response of methane fluxes and methanogen activity to water table and soil warming manipulations in an Alaskan peatland. *J. Geophys. Res. Biogeosci.* **113**(3). http://dx.doi.org/10.1029/2007JG000496.

Vonk J. E., Tank S. E., Bowden W. B., Laurion I., Vincent W. F., Alekseychik P., Amyot M., Billet M. F., Canario J., Cory R. M. and Deshpande B. N. (2015) Reviews and syntheses: effects of permafrost thaw on Arctic aquatic ecosystems. *Biogeosciences* **12**(23), 7129–7167.

Wagai R. and Mayer L. M. (2007) Sorptive stabilization of organic matter in soils by hydrous iron oxides. *Geochim. Cosmochim. Acta* **71**, 25–35. http://dx.doi.org/10.1016/j.gca.2006.08.047.

Walpersdorf E., Koch C. B., Heiberg L., O'Connell D. W., Kjaergaard C. and Hansen H. C. B. (2013) Does vivianite control phosphate solubility in anoxic meadow soils? *Geoderma* **193–194**, 189–199. http://dx.doi.org/10.1016/j.geoderma.2012.10.003.

Weber K. A., Achenbach L. A. and Coates J. D. (2006) Microorganisms pumping iron: anaerobic microbial iron oxidation and reduction. *Nat. Rev. Microbiol.* **4**(10), 752–764. http://dx.doi.org/10.1038/nrmicro1490.

Wiederhold J. G., Kraemer S. M., Teutsch N., Borer P. M., Halliday A. N. and Kretzschmar R. (2006) Iron isotope fractionation during proton-promoted, ligand-controlled, and reductive dissolution of goethite. *Environ. Sci. Technol.* **40**(12), 3787–3793.

Wiseman C. L. S. and Püttmann W. (2006) Interactions between mineral phases in the preservation of soil organic matter. *Geoderma* **134**(1–2), 109–118. http://dx.doi.org/10.1016/j.geoderma.2005.09.001.

Wullschleger S. D., Hinzman L. D. and Wilson C. J. (2011) Planning the next generation of Arctic ecosystem experiments. *EOS* **92**(17), 145. http://dx.doi.org/10.1029/2011EO170006.

Yang Z., Wullschleger S. D., Liang L., Graham D. E. and Gu B. (2016) Effects of warming on the degradation and production of low-molecular-weight labile organic carbon in an Arctic tundra soil. *Soil Biol. Biochem.* **95**, 202–211. http://dx.doi.org/10.1016/j.soilbio.2015.12.022.

Yoshikawa K. and Hinzman L. D. (2003) Shrinking thermokarst ponds and groundwater dynamics in discontinuous permafrost near Council, Alaska. *Permafrost Periglac.* **14**(2), 151–160. http://dx.doi.org/10.1002/ppp.451.

Zak D., Gelbrecht J. and Steinberg C. E. W. (2004) Phosphorus retention at the redox interface of peatlands adjacent to surface waters in Northeast Germany. *Biogeochemistry* **70**(3), 357–368. http://dx.doi.org/10.1007/s10533-003-0895-7.

Zhuang L., Tang J., Wang Y., Hu M. and Zhou S. (2015) Conductive iron oxide minerals accelerate syntrophic cooperation in methanogenic benzoate degradation. *J. Hazard. Mater.* **293**, 37–45.

Zona D., Lipson D. A., Zulueta R. C., Oberbauer S. F. and Oechel W. C. (2011) Microtopographic controls on ecosystem functioning in the Arctic Coastal Plain. *J. Geophys. Res. Biogeosci.* **116**(3), 1–12. http://dx.doi.org/10.1029/2009JG001241.

Zona D., Oechel W. C., Kochendorfer J., Paw U. K. T., Salyuk A. N., Olivas P. C. and Lipson D. A. (2009) Methane fluxes during the initiation of a large-scale water table manipulation experiment in the Alaskan Arctic tundra. *Global Biogeochem. Cycl.* **23**(2), 1–11. http://dx.doi.org/10.1029/2009GB003487.

Associate editor: Owen Duckworth